Plasma membrane nanoscale dynamics of *Arabidopsis* leucine-rich repeat receptor kinase complexes

Michelle von Arx[1,2], Marie-Dominique Jolivet[1,2], David Biermann[1,2], Vaishali Gabani[1], Steven S. Andrews[3], Cyril Zipfel[4,5], Julien Gronnier[1,2,4#]

Correspondence: julien.gronnier@tum.de

1. Plant Cell Biology, TUM School of Life Sciences, Technical University of Munich, Freising, Germany.
2. Center for Plant Molecular Biology (ZMBP), University of Tübingen, Germany.
3. Department of Bioengineering, University of Washington, United states of America.
4. Institute of Plant and Microbial Biology and Zurich-Basel Plant Science Center, University of Zürich, Zürich, Switzerland.
5. The Sainsbury Laboratory, University of East Anglia, Norwich Research Park, Norwich, United Kingdom.

Abstract

Plasma membrane-localized receptors operate as dynamic signaling complexes and integrative networks[1-3], yet the spatial and temporal regulation of these interactions remain largely unknown. Here, by analyzing the components of a minimal *Arabidopsis* leucine-rich repeat receptor kinase network, we describe the differential diffusion and organization of receptor complex components and unveil the nanoscale spatial and temporal logic underlying the formation of receptor kinase complexes. The ligand-binding receptors FLS2 and BRI1, and the accessory receptor BIR3, are organized in plasma membrane nanodomains, within which the co-receptor BAK1 diffuses and is spatially arrested upon ligand perception. BAK1's spatial arrest relies on extracellular domain (ECD)-ECD interactions but does not require receptor complex activation. Mathematical modelling, single molecule imaging and bio-assays infer that accessory receptors maintain a dynamic pool of co-receptors in the vicinity of ligand-binding receptors to promote ligand-induced complex formation and signaling. We propose that ligand-induced receptor kinase complex formation is a deterministic process defined by the relative nanoscale spatial positioning of individual signaling and regulatory components.

Main

Plants and metazoan cell-surface receptors sense and relay a myriad of extracellular signals to coordinate development and adjust to ever-changing environmental conditions[4,5]. In plants, the repertoire of cell-surface receptor kinases has considerably expanded with over 400 members encoded in the genome of *Arabidopsis thaliana* (hereafter Arabidopsis)[6]. Among them, leucine-rich repeat receptor kinases (LRR-RKs) constitute a prominent class that perceive self, non-self

37 and modified-self molecules to regulate development, immunity and reproduction[7-9]. For
38 instance, the ligand-binding LRR-RK BRASSINOSTEROID-INSENSITIVE 1 (BRI1) functions as the
39 main receptor for plant steroid hormones brassinosteroids[7] and forms a complex with the co-
40 receptor BRI1-ASSOCIATED KINASE (BAK1, also called SOMATIC EMBRYOGENESIS RECEPTOR
41 KINASE 3, SERK3) to regulate growth[7,10]. BAK1 also serves as a co-receptor for other LRR-RKs, such
42 as FLAGELING SENSING 2 (FLS2) that sense the flg22 epitope derived from bacterial flagellin to
43 initiate immune signaling[9,11].

44 LRR-RKs have been proposed to function as a coordinated interaction network to process
45 extracellular signals[2]. In this framework, accessory receptor kinases regulate ligand-induced
46 association between ligand-binding receptors and their co-receptors. For instance, the LRR-RK
47 BAK1-INTERACTING RECEPTOR-LIKE KINASE 3 (BIR3) physically associates with BAK1[12,13] and has
48 been proposed to inhibit ligand-induced FLS2-BAK1 and BRI1-BAK1 complex formation[13-15].
49 Several studies have highlighted the spatial organization of LRR-RKs into plasma membrane
50 nanodomains[16-22]. For instance, the spatial separation of FLS2 and BRI1 has been proposed to
51 support signaling specificity[16] and alterations of the nanoscale organization of FLS2 and BAK1
52 correlate with defects in ligand-induced complex formation and signaling[17,23]. Yet, how the
53 dynamic associations of cell surface receptor are coordinated in space and time within the plasma
54 membrane remains unclear. Here, we studied a minimal LRR-RK network composed of the ligand-
55 binding receptors FLS2 and BRI1, their common co-receptor BAK1 and the accessory receptor
56 BIR3.

57 We analyzed the plasma membrane nanoscale organization of FLS2-GFP[24], BRI1-GFP[25] and BAK1-
58 GFP[26] by combining variable-angle total internal reflection microscopy (VA-TIRFM)[27,28] with
59 enhanced super-resolution radial fluctuations (eSRRF)[29] in hypocotyl epidermal cells of light
60 grown Arabidopsis seedlings. Consistent with previous observations made in Arabidopsis
61 cotyledons epidermal cells[16-18,30,31], we observed that FLS2-GFP and BRI1-GFP are organized into
62 well-defined nanodomains (Fig. 1a-b). In contrast, BAK1-GFP showed a more dispersed
63 distribution within the PM (Fig. 1a-b). To complement these observations, we used photochromic
64 reversion, a variant of single-particle tracking photoactivated localization microscopy (spt-PALM)
65 that enables long-term single molecule imaging[32]. We analyzed BRI1, FLS2 and BAK1 tagged with
66 the photoconvertible fluorescence protein mEOS3.2[33] expressed under the control of their native
67 promoter. We observed that FLS2-mEOS3.2 and BRI1-mEOS3.2 are overall static while BAK1 is
68 laterally diffusive and presents a higher diffusion coefficient (Fig. 1c-d; Extended Data Fig. 1a-b).
69 We observed that when transiently expressed in *Nicotiana benthamiana,* or expressed under the
70 control of the *ubiquitin 10* promoter[34] in Arabidopsis stable transgenic lines, FLS2-mEOS3.2
71 remained static and BAK1 remained diffusive (Fig. 1c-d; Extended Data Fig. 1a-d, 2a, 3c). We next
72 analyzed FLS2, BRI1 and BAK1 organization using nanoscale spatiotemporal indexing clustering
73 (NASTIC)[35]. We observed that FLS2 and BRI1 are more clustered than BAK1 (Fig. 1e-f). Together

these observations highlight the differential organization and diffusion of plant LRR-RK complex components, features that contrast with the behavior of animal cell-surface receptors[36-39]. We next investigated the effect of ligand perception on receptor dynamics. We imaged FLS2 and BRI1 within 10 min post ligand-treatment, a time-frame which corresponds to initiation of ligand-induced complex formation and signaling[11,40,41]. In good agreement with the analysis of FLS2-GFP diffusion in *N. benthamiana*[42], we observed that flg22 does not lead to changes in FLS2-mEOS3.2 diffusion in *N. benthamiana* and in Arabidopsis (Fig. 2c-d; Extended Data Fig. 2a-b). Further, flg22 treatment did change FLS2 clustering (Extended Data Fig. 2c-d). Similarly, we observed that BRI1-mEOS3.2 nanoscale dynamics and clustering is unaffected by epi-brassinolide (eBL) treatment (Fig. 2a-b; Extended Data Fig. 2e-f). To corroborate these observations, we used computational analysis of spatial arrests (CASTA)[32] to analyze changes in FLS2 and BRI1 dynamics in long-term single molecule imaging. We observed that flg22 and eBL do not lead to changes in FLS2 and BRI1 spatial arrest (Extended Data Fig. 2g-j). We conclude that ligand-induced complex formation and early ligand-induced signaling is not associated with changes in ligand-binding receptor nanoscale dynamics or organization.

We next examined the behavior of BAK1. We observed that BAK1-mEOS3.2 diffusion coefficient is reduced upon eBL treatment (Fig. 2e-f). Further, we observed an increase in BAK1-mEOS3.2 clustering (Extended Data Fig. 3a-b) and in the frequency of its spatial arrest (Fig. 2i-j) events upon eBL treatment. Similarly, we observed that flg22 treatment reduces BAK1-mEOS3.2 diffusion in *N. benthamiana* (Extended Data Fig. 3c-d). However, in Arabidopsis hypocotyl cells, we did not observe changes in BAK1 mobility behavior (Extended Data Fig. 3e-f). We presumed that the low FLS2 expression in Arabidopsis hypocotyl cells (Extended Data Fig. 1a) combined with the inherent stochasticity of BAK1-mEOS3.2 photoconversion impedes our ability to detect changes in BAK1 mobility behavior. To test this hypothesis, we crossed *bak1-4*/pBAK1::BAK1-mEOS3.2 with Col-0/pFLS2::FLS2-GFP to increase FLS2 accumulation. We observed that introducing FLS2-GFP in *bak1-4*/pBAK1::BAK1-mEOS3.2 leads to detectable flg22-induced decrease in BAK1-mEOS3.2 diffusion (Fig. 2g-h) and increase in BAK1 clustering (Extended Data Fig. 3g-h). Further, we observed that similar to eBL, flg22 treatments lead to an increase in BAK1-mEOS3.2 spatial arrests (Fig. 2i-l). Together these observations show that, while ligand binding RKs are static and organized in clusters independently of exogenous ligand treatment, BAK1 clustering and spatial arrestment increases upon ligand perception. Using dual-color VA-TIRFM we observed that FLS2-GFP and BAK1-mCherry, as well as BRI1-GFP and BAK1-mCherry partially co-localize in control conditions (Extended Data Fig. 4a-b and d-e). These observations are consistent with previous cell surface-selective FLIM analyses of BRI1-GFP and BAK1-mCherry[20], and suggest that BAK1 navigates in the vicinity of ligand-binding receptor nanodomains. Further, we observed that loss of the receptor kinase FERONIA (allele *fer*-4), which induces an increase in BRI1-BAK1 association[43], led to an increased co-localization between BRI1-GFP and BAK1-mCherry (Extended

111 Data Fig. 4f). Similarly, we observed that flg22 treatment leads to an increased co-localization
112 between FLS2-GFP and BAK1-mCherry (Extended Data Fig. 4c). In contrast to BRI1-BAK1, flg22-
113 induced FLS2-BAK1 complex formation was reduced in *fer-4*[44]. In agreement, we observed flg22
114 treatment does not lead to an increase in co-localization between FLS2-GFP and BAK1-mCherry
115 in *fer-4*. Together with single molecule tracking analyses, these observations suggest that BAK1
116 navigates within and is spatially arrested to pre-formed ligand-binding receptor nanodomains
117 upon ligand perception.

118 We next investigated the molecular events underlying ligand-induced BAK1 spatial arrestment.
119 We mutated two residues in the BAK1 ECD, Phenylalanine (F) 60 and F144, which are commonly
120 engaged in interaction with ligand-bound ligand-binding receptors, including BRI1, and are
121 required for ligand-induced complex formation[13,45-48]. We observed that the nanoscale dynamics
122 and organization of BAK1$^{F60A/F144A}$-mEOS3.2 is insensitive to eBL treatment (Fig. 2m; Extended
123 Data Fig. 5a-c), suggesting that ligand-induced BAK1 spatial arrestment relates to ligand-induced
124 complex formation. In agreement, using a BAK1 kinase-dead version of BAK1 (BAK1^{D416N})[49,50], we
125 observed that BAK1 kinase activity is not required for eBL-induced BAK1 spatial arrestment and
126 clustering (Fig. 2n; Extended Data Fig. 5d-f). We conclude that ligand-induced BAK1 spatial
127 arrestment corresponds to ligand-induced complex formation and does not rely on receptor
128 complex activation and downstream signaling events.

129 We observed that a fraction of BAK1 is spatially arrested in absence of exogenous ligand
130 treatment (Fig. 2) and that mutations that abolish BAK1 association with a variety of ligand-
131 binding receptors (Fig. 2m) are not sufficient to abolish BAK1 clustering and spatial arrestment
132 (Extended Data Fig. 5g-i). We thus hypothesized that additional regulators control BAK1 spatial
133 arrestment. The accessory receptor kinase BIR3 physically associates with BAK1[13,14] and is in
134 proximity to FLS2 and BRI1[14]. Using VA-TIRFM-eSRRF we observed that, similar to FLS2 and BRI1
135 (Fig. 1), BIR3-GFP is organized into plasma membrane nanodomains (Extended data Fig. 6a).
136 Corroborating these observations, we observed that BIR3-mEOS3.2 is relatively static and forms
137 nanoclusters (Fig. 3a-d; Extended data Fig. 6b-c). Since BIR3 showed a slow and confined lateral
138 diffusion, we hypothesized that BAK1 transiently physically associates with BIR3 and conditions
139 BAK1 spatial arrestment. We therefore mutated BAK1 Aspartic acid (D) 122, which has been
140 shown to reduce BAK1-BIR3 ECD-ECD interactions *in vitro*[13]. We observed that substituting D122
141 with Alanine (A) led to an increase in BAK1 diffusion (Fig. 3e-f), as well as a reduction in BAK1
142 spatial arrestment (Fig. 3g-h) and clustering (Fig. 3i-j), indicating that BIR3 regulates BAK1
143 nanoscale dynamics. Corroborating these observations, we observed that loss of *BIR3* leads to an
144 increase in BAK1-mEOS3.2 diffusion and a decrease in BAK1 clustering (Extended Data Fig. 7a-e).
145 Loss of *BIR3* was not sufficient to significantly affect BAK1 spatial arrest (Extended Data Fig 7f-g),
146 suggesting the implication of additional factors; potentially the BIR3 paralogues BIR1 and/or
147 BIR2[51,52]. We conclude that the association of BAK1 to BIR3, and potentially other BIRs, contribute

148 to BAK1 clustering and spatial arrestment presumably in the vicinity of the ligand-binding
149 receptor kinases FLS2 and BRI1 (Fig. 3k).

150 We next set to reconstitute the plasma membrane nanoscale dynamics of ligand-induced
151 complex formation *in silico* using particle-based simulations (Fig. 4a)[53]. We used the diffusion
152 parameters extracted from single molecule imaging and known ECD-ECD binding kinetics[13,54] to
153 parametrize our model. These simulations closely recapitulated the nanoscale behavior of single
154 receptor molecules (Extended Data Fig. 8a-c). Interestingly, we observed that introducing BIR3 in
155 these simulations promotes the existence of a dynamic pool of BAK1 in the vicinity of FLS2
156 nanodomains (Fig. 4b-d) and flg22-induced complex formation (Fig. 4e), suggesting that BIR3 has
157 a positive role in regulating ligand-induced complex formation. In agreement, we observed that
158 loss of *BIR3* (*bir3-2* allele[14] and *bir3-c* CRISPR mutant (Extended Data Fig. 7)) led to a decrease in
159 flg22-induced FLS2-BAK1 complex formation in Arabidopsis seedlings (Fig. 4g; Extended Data
160 Figure 9a-c).

161 Corroborating these observations, loss of *BIR3* led to a decrease in flg22-induced MAPK
162 phosphorylation and flg22-induced ROS production (Fig. 4h; Extended Data Fig. 9d-e). These
163 results contrast with a previous report in Arabidopsis[14], but align with the effects of loss of BIRs
164 in wheat[55] and in *N. benthamiana*[56]. In addition, in line with previous observations in Arabidopsis
165 root and dark grown hypocotyls[14], and in rice[57], we observed that loss of *BIR3* led to reduced eBL-
166 responsiveness in light-grown Arabidopsis hypocotyls (Extended Data Fig. 9f, g). These results
167 together indicate that BIR3 functions as positive regulator of both flg22- and eBL-triggered
168 signaling. Altogether, these observations suggest that BIR3 attracts BAK1 in the vicinity of ligand-
169 binding receptors, providing a dynamic pool of BAK1 available for ligand-induced complex
170 formation with ligand-binding receptors. We next tested the effect of increasing the amount of
171 BIR3 *in silico*. These simulations predict a decrease in the number of BAK1 molecules in the
172 vicinity of FLS2 (Fig. 4c). Further, in agreement with the effect of BIR3 over-expression observed
173 *in vivo*[14], increasing the number of BIR3 molecules decreases FLS2-BAK1 complexes formed *in*
174 *silico* (Fig. 4f). In this system, BIR3 predominantly acted as a negative regulator keeping BAK1 away
175 from FLS2 nanodomains. Our data indicate a dual, concentration-dependent, role for the
176 accessory receptor kinase BIR3.

177 **Discussion**

178 How cell surface receptors dynamically assemble into signaling-competent complexes within the
179 plasma membrane remains a fundamental question. By combining super-resolution microscopy,
180 long-term single molecule imaging and mathematical modeling, our results suggest a nanoscale
181 organizational principle underlying the formation of Arabidopsis LRR-RK complexes. Ligand-
182 binding receptors are pre-organized into nanodomains, while the common co-receptor BAK1 is
183 diffusive and spatially arrested to ligand-binding receptors. The spatial and temporal

orchestration of plant LRR-RK and animal cell-surface receptor complexes thus differ. For instance, compared to FLS2 or BRI1, the human epidermal growth factor receptor (EGFR) and type-I interferon receptors are diffusive and undergo ligand-induced dimerization and spatial stabilization[38,58]. Our experimental and *in silico* analyses converge in describing receptor kinases as an organized and predictable system in which BIR3 maintains a dynamic pool of available BAK1 in the vicinity of ligand-binding receptors for ligand-induced complex formation and signaling (Fig. 4i). We thus propose that accessory receptors, such as BIR3, act as spatial regulators for co-receptor availability. This reconciles previously conflicting genetic observations made in several plant species[14,55-57] and highlights how subtle changes in accessory receptor abundance can tune ligand responsiveness. Collectively, our findings suggest that ligand-induced complex formation is a deterministic process defined by the relative spatial positioning of individual signaling and regulatory components at the nanoscale rather than purely stochastic diffusion-driven encounters. In this framework, signaling competence emerges from the pre-established spatial architecture of the plasma membrane and may reflect a general organizational principle of signaling systems.

Acknowledgments

We thank all members of the NanoSignaling Laboratory for fruitful discussions and comments on the manuscript. We thank Niko Geldner for providing the Col-0/pBRI1::BRI1-GFP, Sacco de Vries for providing the Col-0/pBRI1::BRI1-GFP/pBAK1::BAK1-mCherry and Col-0/pBAK1::BAK1-mCherry lines, and Birgit Kemmerling for providing the *bir3-2* mutant. Bio-imaging was performed at the ZMBP microscopy facility. We thank Sven zur Oven-Krockhaus for maintaining the VA-TIRFM. We thank Birgit Kemmerling, Thorsten Nürnberger and Kyle Bender for comments on the manuscript. This research was supported by the Deutsche Forschungsgemeinschaft (DFG) grants (A09-SFB1101 and B01-TRR356) to J.G., the European Molecular Biology Organization (postdoctoral fellowship EMBO LTF 438-2018, to J.G.), the European Research Council under the European Union's Horizon 2020 research and innovation programme grant agreement no. 773153 (project 'IMMUNO-PEPTALK' to C.Z.), the University of Zürich (to C.Z.), the University of Tübingen (to J.G.) and the Technical University of Munich (to J.G.).

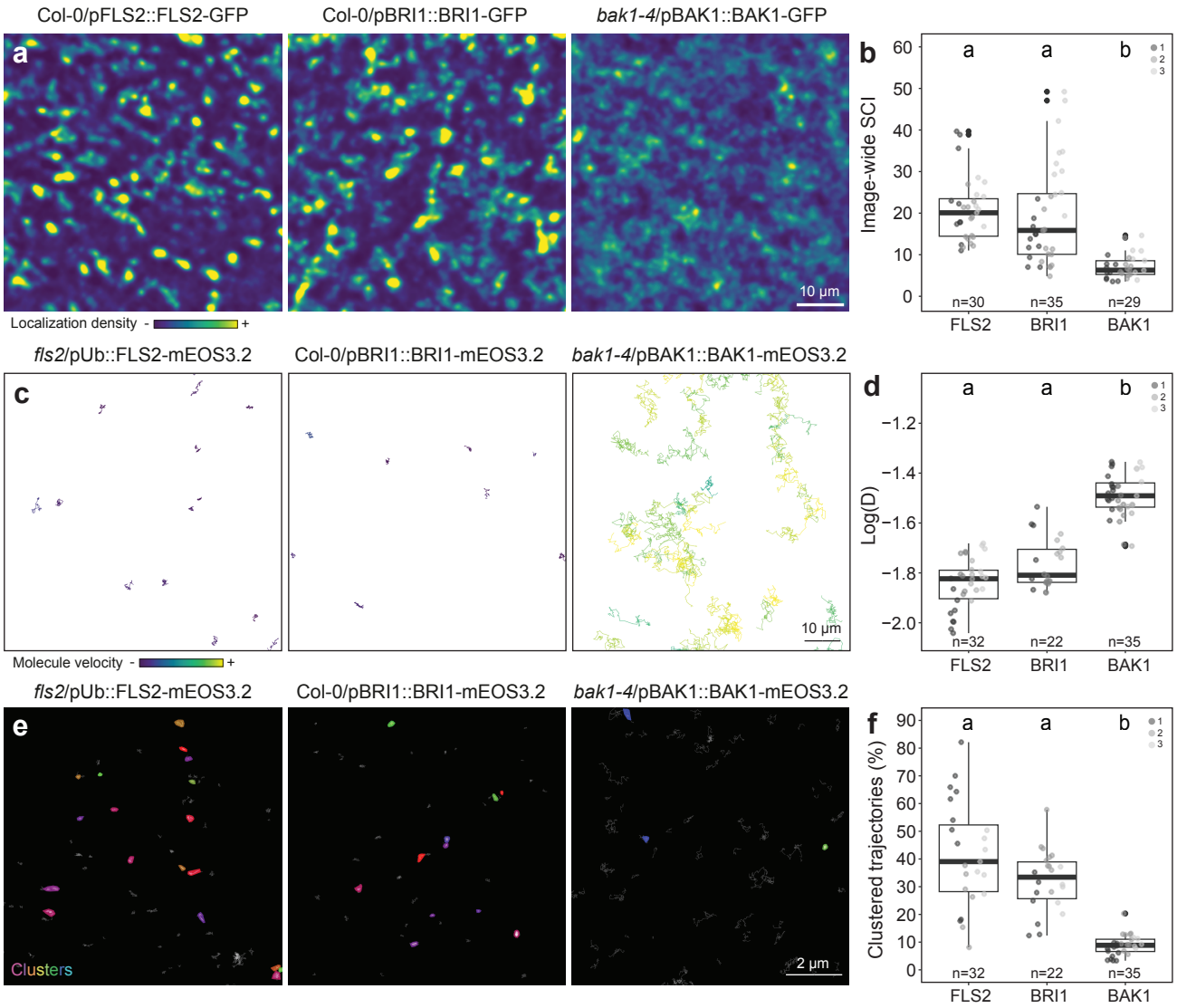
Col-0/pFLS2::FLS2-GFP
Col-0/pBRI1::BRI1-GFP
bak1-4/pBAK1::BAK1-GFP
a
10 µm
Localization density - +
b
Image-wide SCI
a
a
b
n=30
n=35
n=29
FLS2
BRI1
BAK1
fls2/pUb::FLS2-mEOS3.2
Col-0/pBRI1::BRI1-mEOS3.2
bak1-4/pBAK1::BAK1-mEOS3.2
c
10 µm
Molecule velocity - +
d
Log(D)
n=32
n=22
n=35
fls2/pUb::FLS2-mEOS3.2
Col-0/pBRI1::BRI1-mEOS3.2
bak1-4/pBAK1::BAK1-mEOS3.2
e
Clusters
2 µm
f
Clustered trajectories (%)
n=32
n=22
n=35

Figures legends

Figure 1 | Differential organization and dynamics of LRR-RK complex components.

a, Representative eSRRF images of FLS2-GFP, BRI1-GFP and BAK1-GFP plasma membrane organization in 5-day-old Arabidopsis hypocotyl. **b**, Quantification of the image wide spatial clustering index (iSCI). Each data point represents the average value per cell (n), colors indicate independent experiments. **c**, Representative images of FLS2-mEOS3.2, BRI1-mEOS3.2 and BAK1-mEOS3.2 long-term single molecule trajectories in 5-day-old Arabidopsis hypocotyl. Trajectories are colored based on velocity. **d**, Analysis of instantaneous diffusion coefficient (D). Each data point represents the average log(D) value in $\mu m^2/s$ obtained per cell (n), colors indicate independent experiments. **e**, Representative images of FLS2-mEOS3.2, BRI1-mEOS3.2 and BAK1-mEOS3.2 trajectories nanoclustering in 5-day-old Arabidopsis hypocotyl. **f**, Quantification of percentage of clustered trajectories. Each data point represents the percentage of clustered trajectories per cell (n), colors indicate independent experiments. Conditions sharing a letter are not significantly different in pairwise Wilcoxon with Bonferroni correction ($p>0.05$).

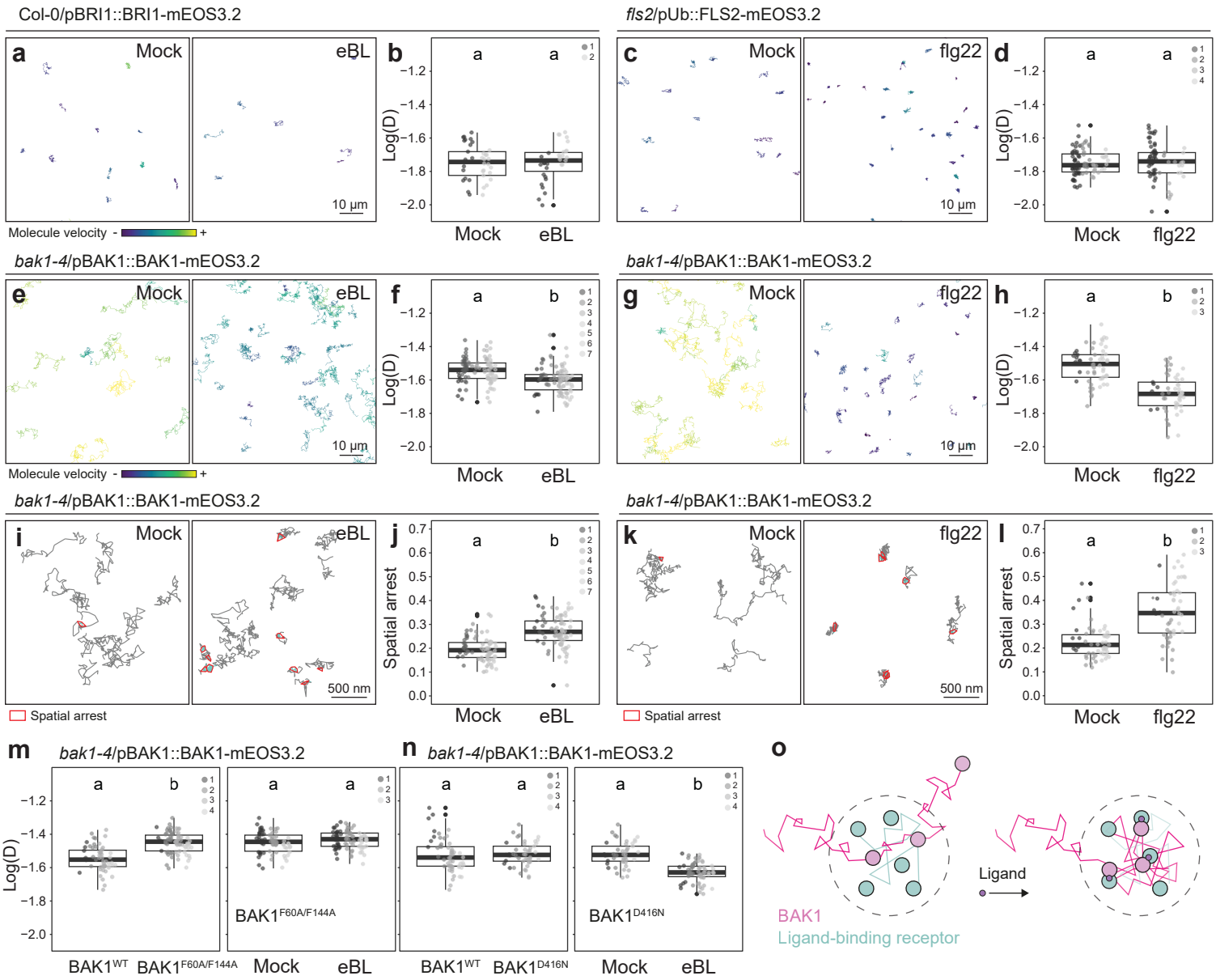
Col-0/pBRI1::BRI1-mEOS3.2
fls2/pUb::FLS2-mEOS3.2
a
Mock
eBL
10 µm
Molecule velocity - +
b
Log(D)
Mock
eBL
c
flg22
d
bak1-4/pBAK1::BAK1-mEOS3.2
e
f
g
h
i
500 nm
Spatial arrest
j
Spatial arrest
k
l
m
n
BAK1F60A/F144A
BAK1D416N
BAK1WT
o
Ligand
BAK1
Ligand-binding receptor

230 **Figure 2 | BAK1 is spatially arrested upon ligand perception.**
231 **a**, Representative BRI1-mEOS3.2 trajectories, long-term single molecule imaging in presence of 1
232 µM eBL or corresponding mock control (EtOH) in Arabidopsis hypocotyl. **b**, Quantification of
233 instantaneous diffusion coefficient (D) within 10 min of treatment. Each data point represents the
234 average log(D) value obtained per cell (n), colors indicate independent experiments. **c**,
235 Representative FLS2-mEOS3.2 trajectories, long-term single molecule imaging in presence of 1
236 µM flg22 or corresponding mock control (H_2O) in Arabidopsis hypocotyl. **d**, Quantification of
237 instantaneous diffusion coefficient (D) within 10 min of treatment. Each data point represents the
238 average log(D) value obtained per cell (n), colors indicate independent experiments. **e**, **g**, **i**, and **k**,
239 Representative BAK1-mEOS3.2 trajectories, long-term single molecule imaging in presence of 1
240 µM eBL (**e** and **i**) or 1 µM flg22 (**g** and **k**) or the corresponding mock controls (EtOH or H_2O) in
241 *bak1-4* (**e** and **i**) and *bak1-4*/pFLS2::FLS2-GFP (**g** and **k**) hypocotyls. **f**, **h**, **m** and **n**, Quantification
242 of instantaneous diffusion coefficient (D) within 10 min of treatment. Each data point represents
243 the average log(D) value obtained per cell (n), colors indicate independent experiments. **j** and **l**,
244 Quantification of BAK1-mEOS3.2 spatial arrests within 10 min of treatment. Each data point
245 represents the average number of spatial arrests per trajectory obtained per cell (n), colors
246 indicate independent experiments. Conditions sharing a letter are not significantly different in
247 pairwise Wilcoxon test with Bonferroni correction ($p>0.05$). **o**, Working model: BAK1 navigates
248 within and is stabilized to pre-formed ligand-binding RK nanodomains upon ligand perception.
249

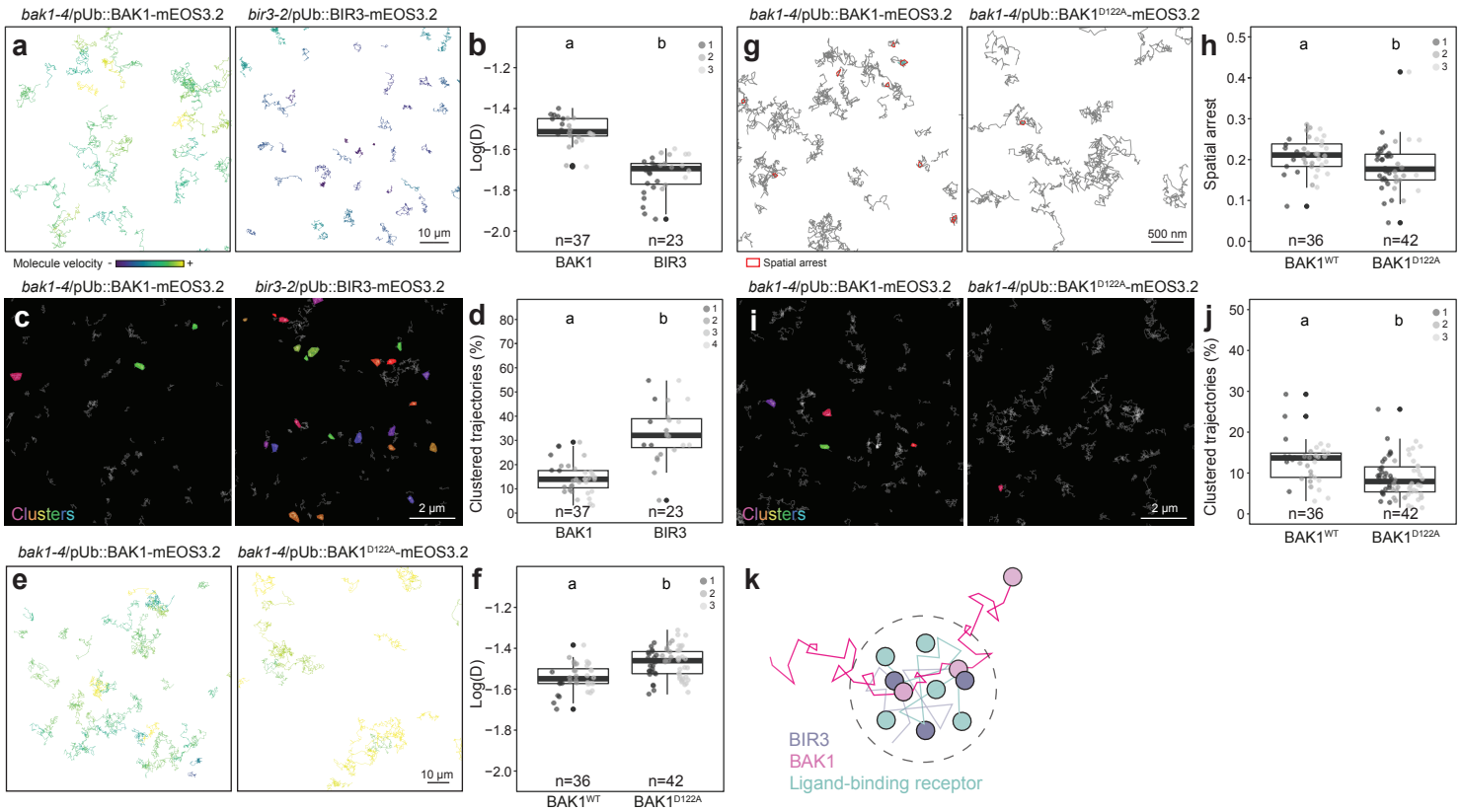
bak1-4/pUb::BAK1-mEOS3.2
bir3-2/pUb::BIR3-mEOS3.2
a
10 µm
Molecule velocity - +
b
Log(D)
n=37
n=23
BAK1
BIR3
bak1-4/pUb::BAK1-mEOS3.2
bak1-4/pUb::BAK1D122A-mEOS3.2
g
500 nm
Spatial arrest
h
Spatial arrest
n=36
n=42
BAK1WT
BAK1D122A
c
Clusters
2 µm
d
Clustered trajectories (%)
e
f
i
j
k
BIR3
BAK1
Ligand-binding receptor

250 **Figure 3 | BIRs regulates BAK1 plasma membrane nanoscale dynamics.**
251 **a** and **e**, Representative BAK1-mEOS3.2 and BIR3-mESO3.2 (**a**) or BAK1-mEOS3.2 and BAK1^{D122A}-
252 mEOS3.2 (**e**) trajectories, long-term single molecule imaging, colors indicate velocity. **b** and **f**,
253 Quantification of instantaneous diffusion coefficient (D). Each data point represents the average
254 log(D) value obtained per cell (n), colors indicate independent experiments. **c** and **i**,
255 Representative images of BAK1-mEOS3.2. and BIR3-mEOS3.2 (**c**) or BAK1-mEOS3.2 and BAK1^{D122A}-
256 mEOS3.2 (**i**) trajectories nanoclustering. **d** and **j**, Quantification of clustered trajectories. Each data
257 point represents the percentage of clustered trajectories per cell (n), colors indicate independent
258 experiments. **g**, Representative images of BAK1-mEOS3.2 and BAK1^{D122A}-mEOS3.2 spatial arrest.
259 **h**, Quantification of BAK1-mEOS3.2 and BAK1^{D122A}-mEOS3.2 spatial arrests. Each data point
260 represents the average number of spatial arrests per trajectory obtained per cell (n), colors
261 indicate independent experiments. Conditions sharing a letter are not significantly different in
262 pairwise Wilcoxon with Bonferroni correction ($p>0.05$). **k**, Working model: pre-formed ligand-
263 binding RK nanodomains contain accessory RKs such as BIR3.
264

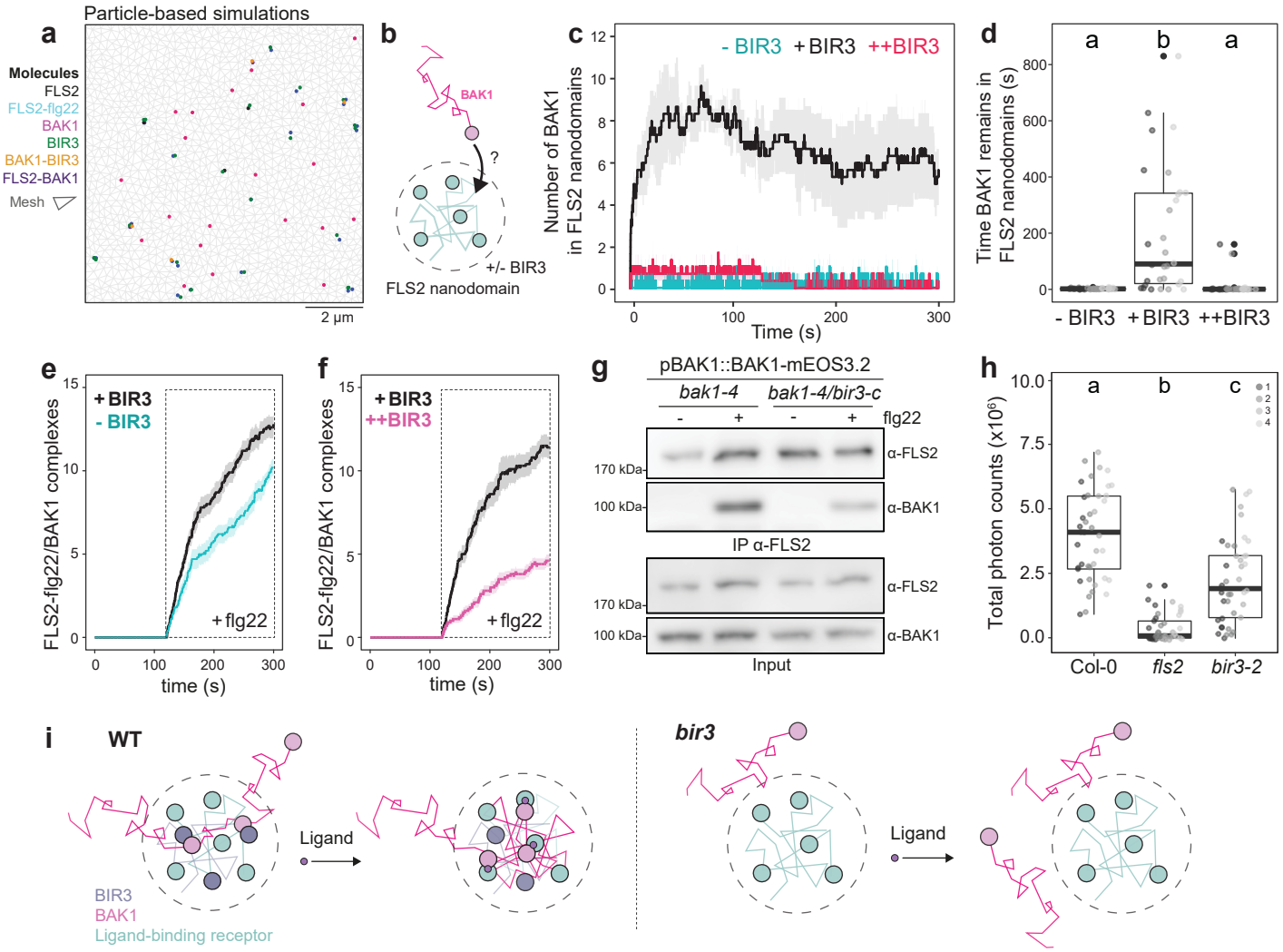
Particle-based simulations
a
Molecules
FLS2
FLS2-flg22
BAK1
BIR3
BAK1-BIR3
FLS2-BAK1
Mesh
2 µm
b
BAK1
?
+/- BIR3
FLS2 nanodomain
c
- BIR3 + BIR3 ++BIR3
Number of BAK1 in FLS2 nanodomains
Time (s)
d
Time BAK1 remains in FLS2 nanodomains (s)
- BIR3 + BIR3 ++BIR3
e
+ BIR3
- BIR3
+ flg22
FLS2-flg22/BAK1 complexes
time (s)
f
+ BIR3
++BIR3
+ flg22
FLS2-flg22/BAK1 complexes
time (s)
g
pBAK1::BAK1-mEOS3.2
bak1-4
bak1-4/bir3-c
flg22
170 kDa
100 kDa
α-FLS2
α-BAK1
IP α-FLS2
Input
h
Total photon counts (x10⁶)
Col-0
fls2
bir3-2

i
WT
Ligand
BIR3
BAK1
Ligand-binding receptor
bir3
Ligand

265 **Figure 4 | BIR3 maintains a dynamic pool of BAK1 close to FLS2 for ligand-induced complex**
266 **formation.**
267 **a**, Snapshot of a particle-based simulation. **b,** Schematic depicting of the monitoring of BAK1
268 occurrence in FLS2 nanodomain in presence and absence of BIR3 in particle-based simulations. **c**,
269 Number of BAK1 molecules present in FLS2 nanodomains over time. Data show mean ± se of 3
270 independent simulations. **d**, Duration of BAK1 occurrence in FLS2 nanodomains. Data points
271 correspond to individual FLS2 nanodomain entry events, colors indicate independent simulations.
272 **e-f,** Analysis of FLS2-flg22/BAK1 complex formation over time in presence of intermediate levels
273 of BIR3 (+BIR3), no BIR3 (-BIR3) (**e**) or high levels of BIR3 (++BIR3) (**f**). The simulations were run
274 120 s prior to the addition of flg22 in the system. Data represent mean ± se of 10 independent
275 simulations per scenario. **g**, Immunoprecipitation of FLS2 in *bak1-4*/pBAK1::BAK1-mEOS3.2 or
276 *bir3-c*/*bak1-4*/pBAK1::BAK1-mEOS3.2 CRISPR line after treatment with 20 nM flg22 or
277 corresponding mock solution (H_2O) for 2 min. Membranes were probed with anti-FLS2 or anti-
278 BAK1. **h**, Reactive oxygen species production (ROS) in 4-week-old Arabidopsis leaf discs elicited
279 with 100 nM flg22. Data points indicate total photon counts measured in individual leaf discs (n),
280 colors indicate independent experiments. Conditions sharing a letter are not significantly different
281 in pairwise Wilcoxon test with Bonferroni correction ($p<0.05$). **i**, Working model: In WT conditions
282 BIR3 attracts and maintains a dynamic pool of BAK1 for efficient ligand-induced complex
283 formation. In absence of accessory receptors, such as BIR3, BAK1 is not maintained in the vicinity
284 of ligand-binding receptors, and the likelihood of ligand-induced complexes is reduced.
285

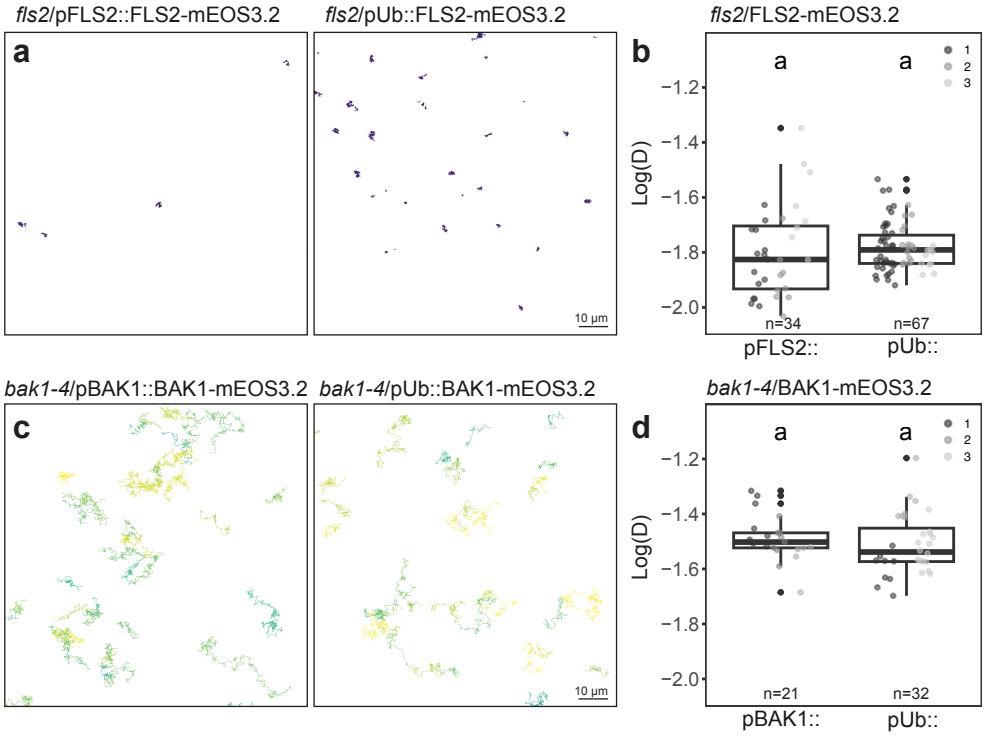
fls2/pFLS2::FLS2-mEOS3.2
fls2/pUb::FLS2-mEOS3.2
a
10 µm
fls2/FLS2-mEOS3.2
b
a
a
1
2
3
Log(D)
−1.2
−1.4
−1.6
−1.8
−2.0
n=34
n=67
pFLS2::
pUb::
bak1-4/pBAK1::BAK1-mEOS3.2
bak1-4/pUb::BAK1-mEOS3.2
c
10 µm
bak1-4/BAK1-mEOS3.2
d
a
a
1
2
3
Log(D)
−1.2
−1.4
−1.6
−1.8
−2.0
n=21
n=32
pBAK1::
pUb::

286 **Extended Data Figure 1 | Analysis of FLS2 and BAK1 diffusion in Arabidopsis**
287 **a** and **c**, Representative single molecule trajectories of FLS2-mEOS3-2 and BAK1-mEOS3.2, long-
288 term single molecule imaging in Arabidopsis hypocotyl epidermis, colors indicate velocity. **b** and
289 **d**, Quantification of instantaneous diffusion coefficient (D). Each data point represents the
290 average log(D) value obtained per cell (n). Conditions sharing a letter are not significantly different
291 in pairwise Wilcoxon test with Bonferroni correction ($p<0.05$).
292

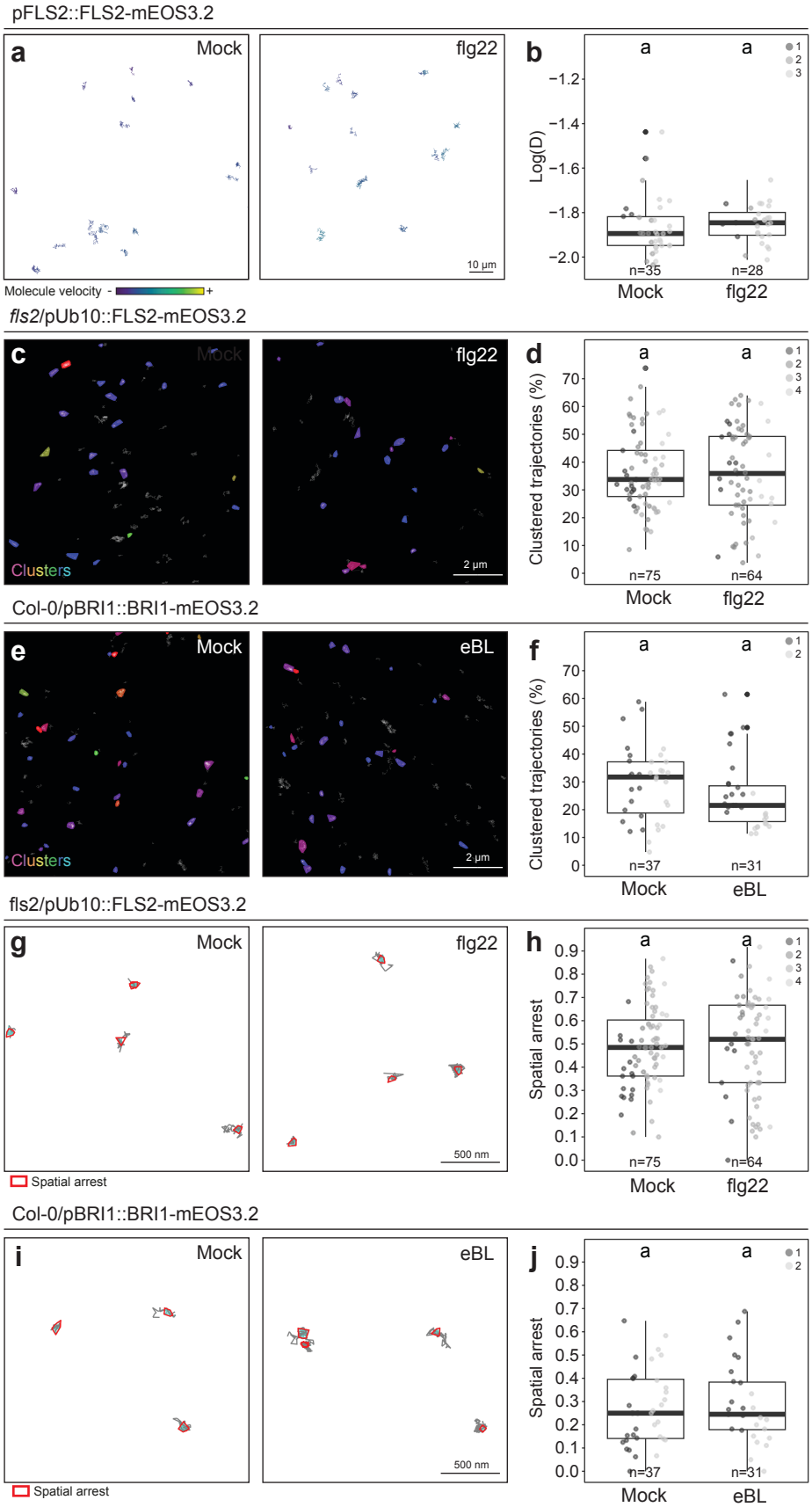
pFLS2::FLS2-mEOS3.2
a
Mock
flg22
10 µm
Molecule velocity - +
b
Log(D)
n=35
n=28
Mock
flg22
fls2/pUb10::FLS2-mEOS3.2
c
Clusters
2 µm
d
Clustered trajectories (%)
n=75
n=64
Col-0/pBRI1::BRI1-mEOS3.2
e
eBL
f
n=37
n=31
fls2/pUb10::FLS2-mEOS3.2
g
500 nm
Spatial arrest
h
Spatial arrest
Col-0/pBRI1::BRI1-mEOS3.2
i
j

293 **Extended Data Figure 2 | Analysis of FLS2 and BRI1 diffusion and organization in presence and**
294 **absence of exogenous ligand treatment.**
295 **a,** Representative single molecule trajectories of FLS2-mEOS3.2 in presence of 1 µM flg22 or
296 corresponding mock control (H_2O) in *N. benthamiana*. **b**, Quantification of instantaneous
297 diffusion coefficient (D) within 10 min of treatment. Each data point represents the average log(D)
298 value obtained per cell (n), colors indicate independent experiments. **c, e, g, i,** Representative
299 images of FLS2-mEOS3.2 (**c, g**) or BRI1-mEOS3.2 (**e, i**) single molecule nanoclustering (**c, e**) or
300 trajectories spatial arrest (**g, i**) in Arabidopsis hypocotyl in presence of 1 µM flg22 (**c, g**) or 1 µM
301 eBL (**e, i**) or the corresponding mock controls (H_2O or EtOH). **d** and **f**, Quantification of FLS2-
302 mEOS3.2 (**d**) or BRI1-mEOS3.2 (**f**) of clustered trajectories within 10 min of treatment. Each data
303 point represents the percentage of clustered trajectories per cell (n), colors indicate independent
304 experiments. Conditions sharing a letter are not significantly different in pairwise Wilcoxon with
305 Bonferroni correction ($p>0.05$). **h** and **j,** Quantification of FLS2-mEOS3.2 (**h**) or BRI1-mEOS3.2 (**j**)
306 spatial arrest within 10 min of treatment. Each data point represents the average number of
307 spatial arrests per trajectory obtained per cell (n), colors indicate independent experiments
308

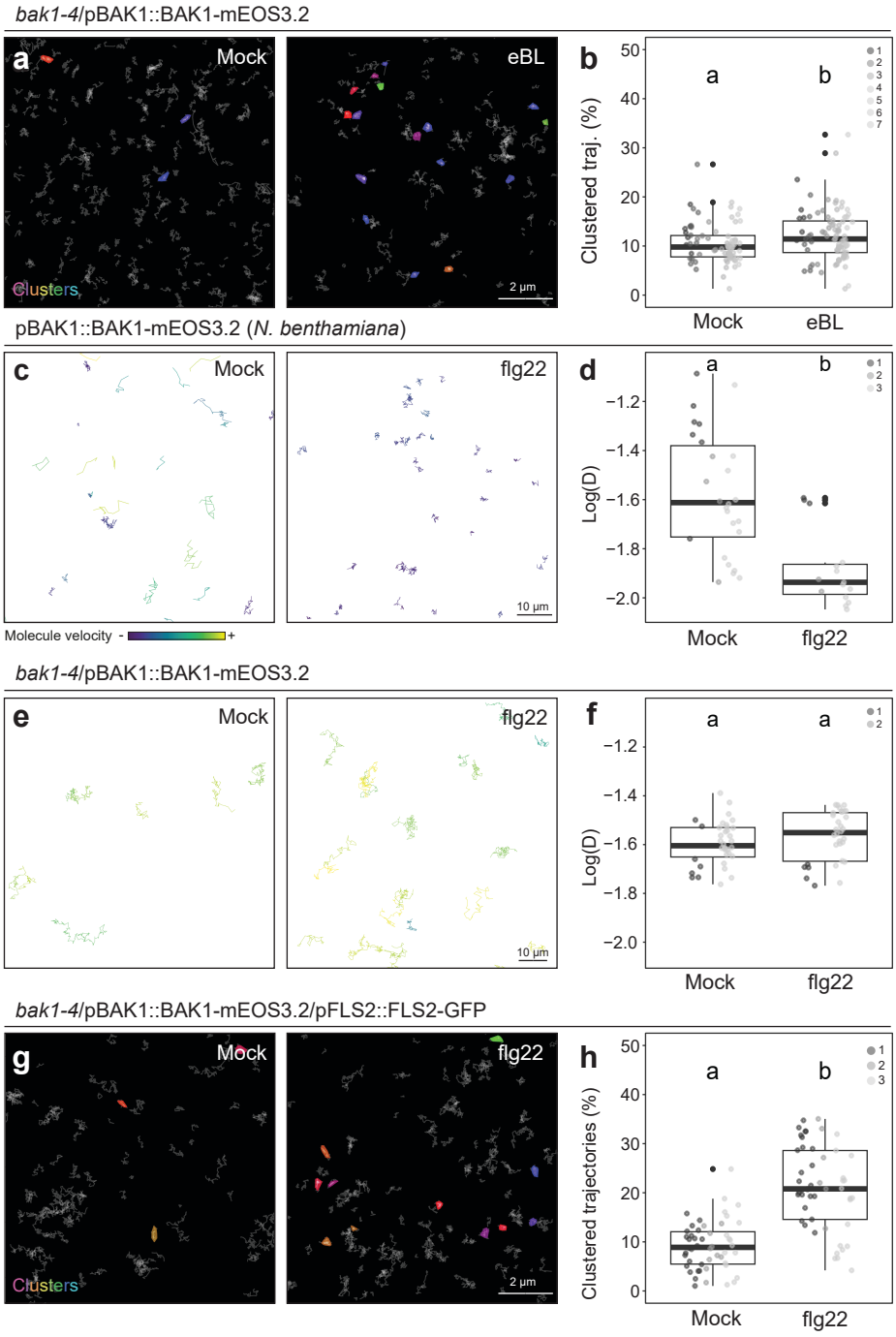
bak1-4/pBAK1::BAK1-mEOS3.2
a
Mock
eBL
Clusters
2 µm
b
Clustered traj. (%)
a
b
Mock
eBL
pBAK1::BAK1-mEOS3.2 (N. benthamiana)
c
Mock
flg22
10 µm
Molecule velocity
d
Log(D)
a
b
Mock
flg22
bak1-4/pBAK1::BAK1-mEOS3.2
e
Mock
flg22
10 µm
f
Log(D)
a
a
Mock
flg22
bak1-4/pBAK1::BAK1-mEOS3.2/pFLS2::FLS2-GFP
g
Mock
flg22
Clusters
2 µm
h
Clustered trajectories (%)
a
b
Mock
flg22

309 **Extended Data Figure 3 | Analysis of BAK1 diffusion and organization in presence and absence**
310 **of exogenous ligand treatment.**
311 **a** and **g**, Representative images of BAK1-mEOS3.2 trajectories nanoclustering in Arabidopsis
312 hypocotyl in presence of 1 µM eBL (**a**) or 1 µM flg22 (**g**) or the corresponding mock controls (EtOH
313 or H_2O) in *bak1-4* (**a**) and *bak1-4*/pFLS2::FLS2-GFP (**g**). **b** and **h**, Quantification of clustered
314 trajectories within 10 min of treatment. Each data point represents the percentage of clustered
315 trajectories per cell (n), colors indicate independent experiments. **c** and **e**, Representative BAK1-
316 mEOS3.2 trajectories in presence of 1 µM flg22 or the corresponding mock control (H_2O)
317 expressed in *N. benthamiana* leaves (**c**) or stably expressed in Arabidopsis hypocotyl (**e**). **d** and **f,**
318 Quantification of instantaneous diffusion coefficient (D) within 10 min of treatment. Each data
319 point represents the average log(D) value obtained per cell (n), colors indicate independent
320 experiments. Conditions sharing a letter are not significantly different in pairwise Wilcoxon test
321 with Bonferroni correction ($p<0.05$).
322

pFLS2::FLS2-GFP/pBAK1::BAK1-mCherry

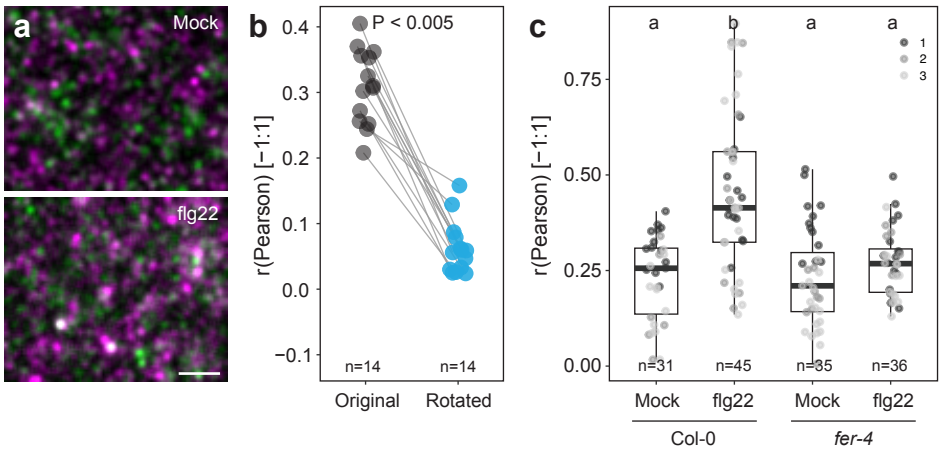

pBRI1::BRI1-GFP/pBAK1::BAK1-mCherry

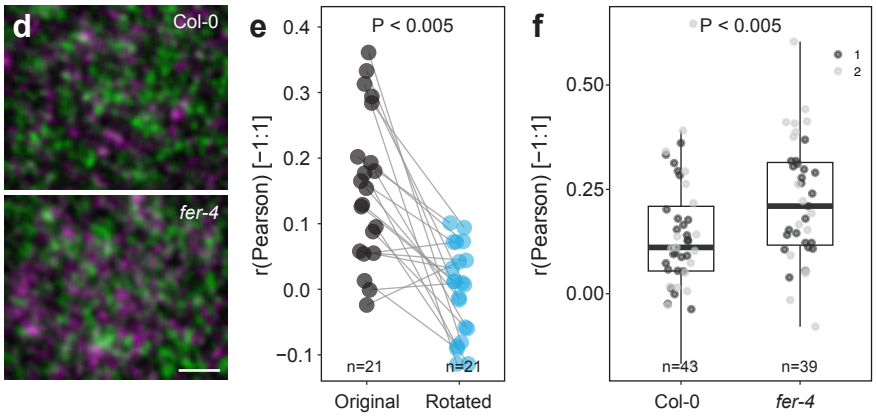

323 **Extended Data Figure 4 | Analysis of FLS2-BAK1 and BRI1-BAK1 co-localization.**
324 **a** and **d**, Representative VA-TIRFM images of FLS2-GFP and BAK1-mCherry (**a**), and BRI1-GFP and
325 BAK1-mCherry. **b** and **e**, Quantification of the co-localization between FLS2-GFP and BAK1-
326 mCherry (**b**) and between BRI1-GFP and BAK1-mCherry (**e**). Each data point represents Pearson
327 correlation coefficient for individual cells (n), lines connect raw and corresponding control
328 rotated (90° mCherry) images. **c** and **f**, Quantification of the co-localization between FLS2-GFP
329 and BAK1-mCherry (**c**) and between BRI1-GFP and BAK1-mCherry (**f**), in presence of 1 µM flg22
330 or the corresponding mock control (H_2O) (**c**) or control condition (f) in WT Col-0 or *fer-4*. Each
331 data point represents the average Pearson correlation coefficient for individual cells (n), colors
332 indicate independent experiments. Conditions which do not share a letter are significantly
333 different in pairwise Wilcoxon test with Bonferroni p-value adjustment ($p < 0,05$).
334

bak1-4/pBAK1::BAK1$^{F60A/F144A}$-mEOS3.2

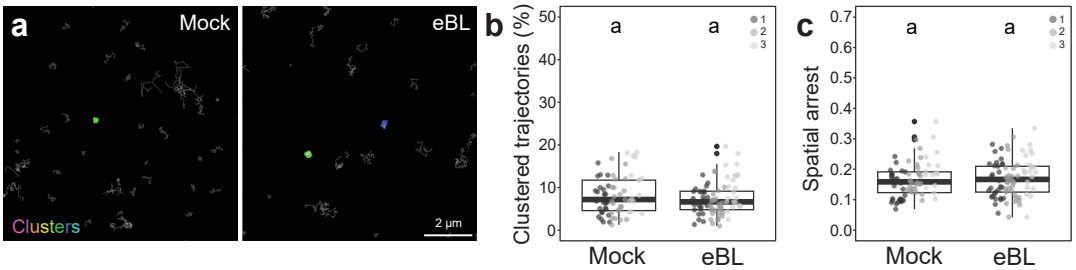

bak1-4/pBAK1::BAK1^{D416N}-mEOS3.2

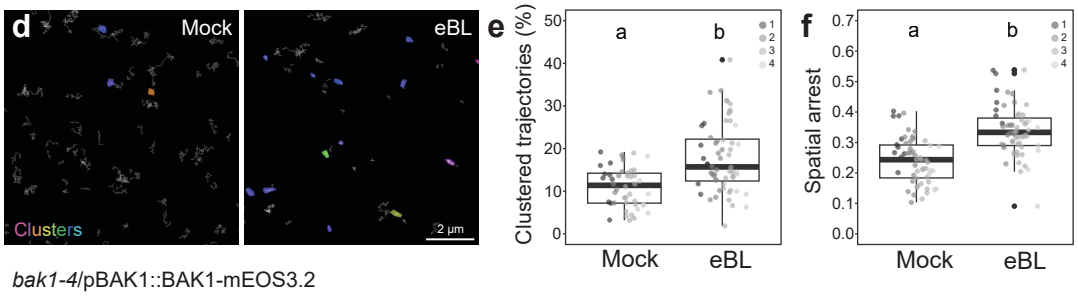

bak1-4/pBAK1::BAK1-mEOS3.2

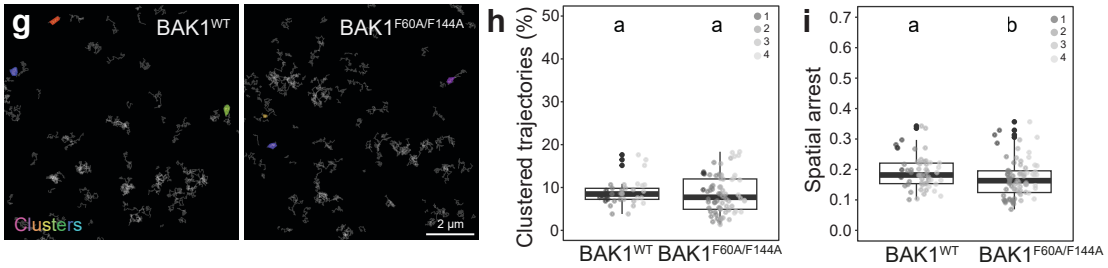

335 **Extended Data Figure 5 | Analysis of the organization of BAK1 mutants in presence and absence**
336 **of exogenous eBL treatment.**
337 **a, d** and **g**, Representative single molecule trajectories clustering of $BAK1^{F60AF144A}$-mEOS3.2 (**a**),
338 $BAK1^{D416N}$-mEOS3.2 (**d**) or $BAK1^{WT}$-mEOS3.2 and $BAK1^{F60AF144A}$-mEOS3.2 (**g**) in presence of 1 µM
339 eBL (**a** and **d**) or the corresponding mock control (EtOH) (**a, d** and **g**). **b, e** and **h**, Quantification
340 clustered trajectories within 10 min of treatment. Each data point represents the percentage of
341 clustered trajectories per cell (n), colors indicate independent experiments. **c, f** and **i**,
342 Quantification of $BAK1^{F60AF144A}$-mEOS3.2 (**c**), $BAK1^{D416N}$-mEOS3.2 (**f**) or $BAK1^{WT}$-mEOS3.2 and
343 $BAK1^{F60AF144A}$-mEOS3.2 (**i**) spatial arrest within 10 min of treatment. Each data point represents
344 the percentage of clustered trajectories per cell (n), colors indicate independent experiments.
345 Conditions sharing a letter are not significantly different in pairwise Wilcoxon test with Bonferroni
346 correction ($p<0.05$).
347

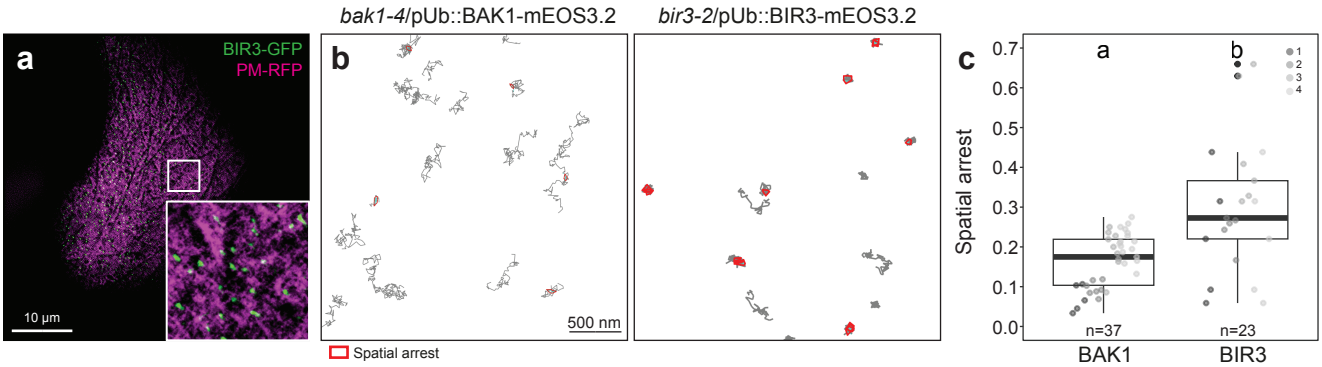
a
BIR3-GFP
PM-RFP
10 µm
bak1-4/pUb::BAK1-mEOS3.2
bir3-2/pUb::BIR3-mEOS3.2
b
500 nm
Spatial arrest
c
Spatial arrest
0.0
0.1
0.2
0.3
0.4
0.5
0.6
0.7
a
b
1
2
3
4
n=37
n=23
BAK1
BIR3

348 **Extended Data Figure 6 | Analysis of BIR3 organization and diffusion.**
349 **a**, Representative eSRRF images of BIR3-GFP control plasma membrane (PM) protein expressed
350 in *N. benthamiana*. **b**, Representative single molecule trajectories of BAK1-mEOS3.2 and BIR3-
351 mESO3.2, long term single molecule imaging in Arabidopsis hypocotyl. **c**, Quantification of spatial
352 arrests. Each data point represents the average number of spatial arrests per trajectory obtained
353 per cell (n), colors indicate independent experiments. Conditions sharing a letter are not
354 significantly different in pairwise Wilcoxon test with Bonferroni correction ($p<0.05$).
355

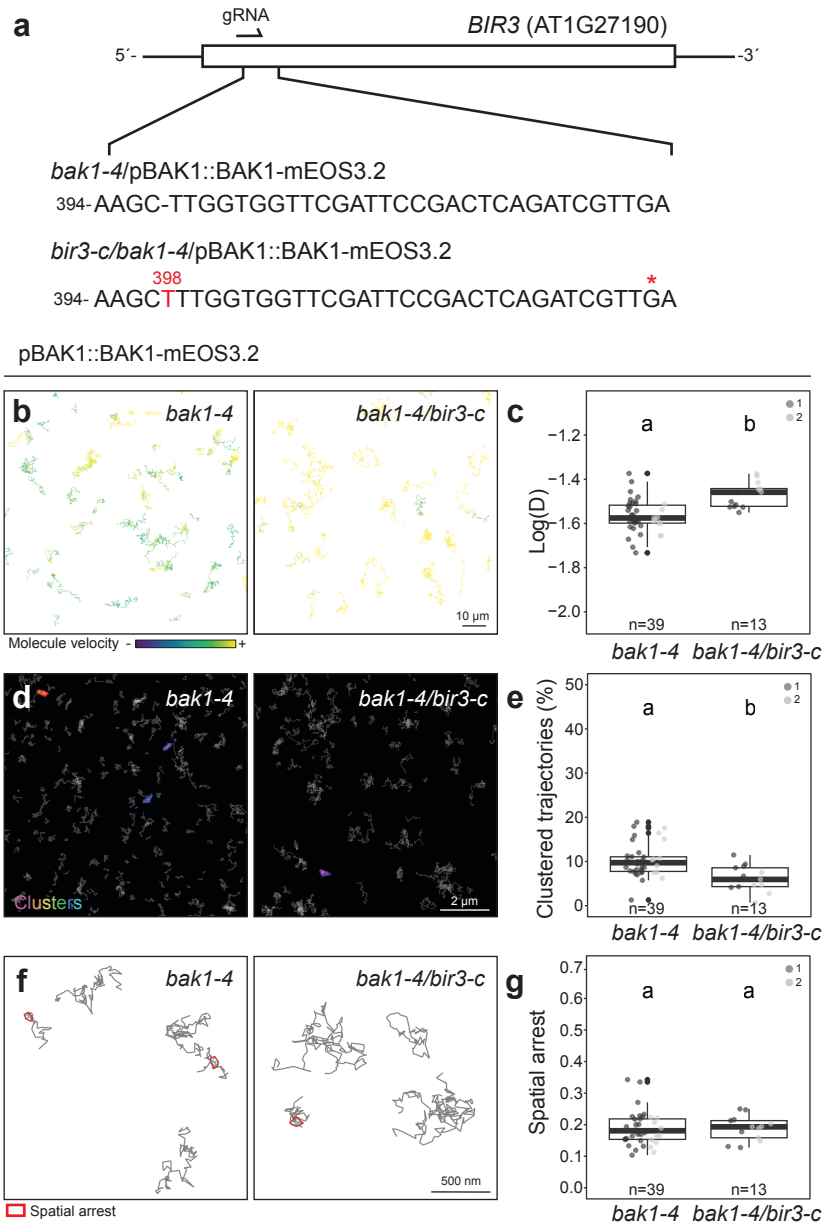
a
gRNA
BIR3 (AT1G27190)
5´-
-3´
bak1-4/pBAK1::BAK1-mEOS3.2
394- AAGC-TTGGTGGTTCGATTCCGACTCAGATCGTTGA
bir3-c/bak1-4/pBAK1::BAK1-mEOS3.2
398
394- AAGCTTTGGTGGTTCGATTCCGACTCAGATCGTTGA
*
pBAK1::BAK1-mEOS3.2
b
bak1-4
bak1-4/bir3-c
10 µm
Molecule velocity - +
c
Log(D)
a
b
n=39
n=13
bak1-4
bak1-4/bir3-c
d
bak1-4
bak1-4/bir3-c
Clusters
2 µm
e
Clustered trajectories (%)
a
b
n=39
n=13
bak1-4
bak1-4/bir3-c
f
bak1-4
bak1-4/bir3-c
500 nm
Spatial arrest
g
Spatial arrest
a
a
n=39
n=13
bak1-4
bak1-4/bir3-c

356 **Extended Data Figure 7| Analysis of BAK1 diffusion and organization in a *BIR3* CRISPR mutant**
357 **a**, Schematic describing the *bir3-c*/*bak1-4*/pBAK1::BAK1-mEOS3.2 CRISPR line. The number of
358 base pairs from the start codon is indicated. Red letters represent insertions observed in gDNA
359 sequencing. Asterisks indicate early stop codons. **b, d, f**. Representative trajectories of BAK1-
360 mEOS3.2, long-term single molecule imaging in *bak1-4* or *bak1-4*/*bir3-c* Arabidopsis hypocotyls.
361 **c**, Quantification of instantaneous diffusion coefficient (D). Each data point represents the average
362 log(D) value obtained per cell (n), colors indicate independent experiments. **e**, Quantification of
363 clustered trajectories. Each data point represents the percentage of clustered trajectories per cell
364 (n), colors indicate independent experiments. **g**, Quantification of spatial arrests. Each data point
365 represents the average number of spatial arrests per trajectory obtained per cell (n), colors
366 indicate independent experiments. Conditions sharing a letter are not significantly different in
367 pairwise Wilcoxon test with Bonferroni correction ($p>0.05$).
368

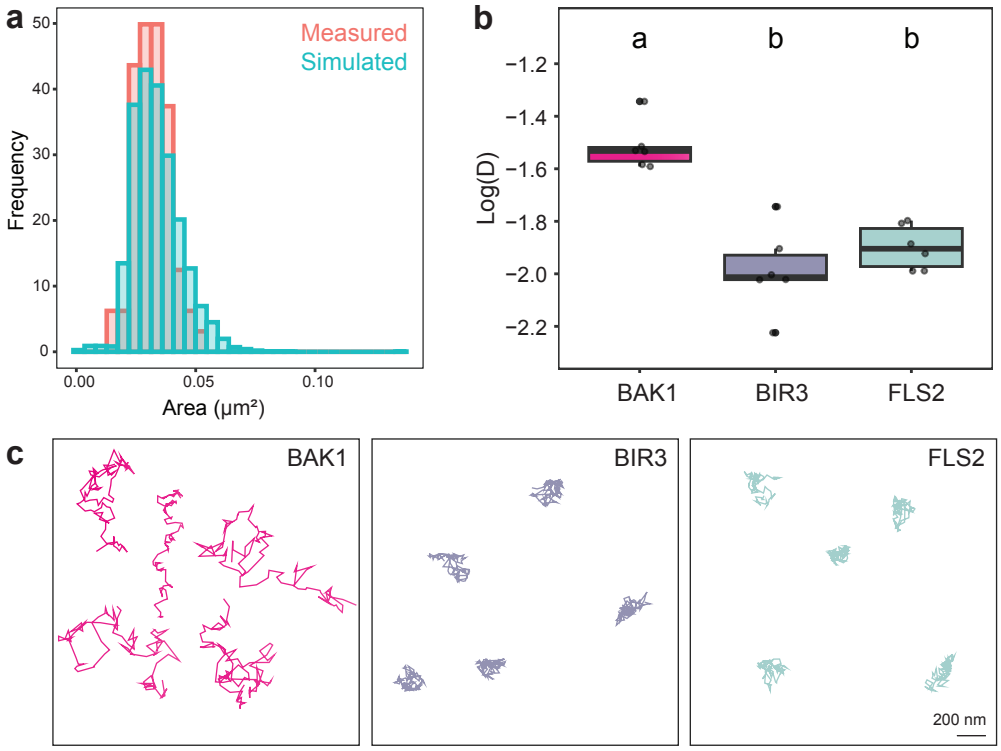
a
Measured
Simulated
Frequency
Area (μm²)
b
a
b
b
Log(D)
BAK1
BIR3
FLS2
c
BAK1
BIR3
FLS2
200 nm

Extended Data Figure 8| Particle-based simulation recapitulates native protein behavior. **a**, Quantification of the area of simulated FLS2 confinement zones (blue) and measured FLS2-mEOS3.2 nanoclusters observed by spt-PALM and analysed by NASTIC (red). **b**, Quantification of instantaneous diffusion coefficient (D) of simulated BAK1, FLS2 and BIR3 molecules. Conditions sharing a letter are not significantly different in pairwise Wilcoxon test with Bonferroni correction ($p<0.05$). **c**, Representative single molecule tracks of simulated BAK1, FLS2 and BIR3 molecules.

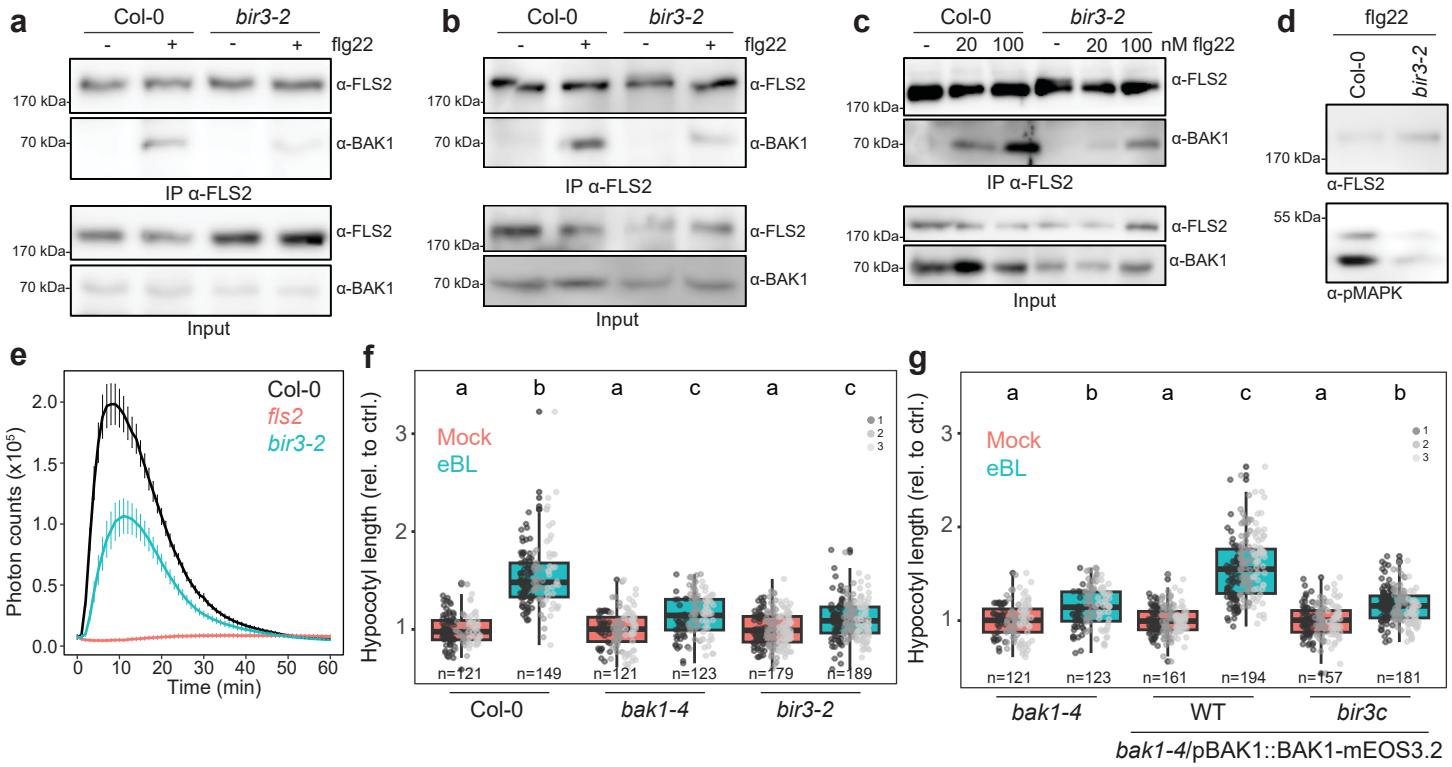
a
Col-0
bir3-2
flg22
170 kDa
70 kDa
α-FLS2
α-BAK1
IP α-FLS2
Input
b
c
nM flg22
d
55 kDa
α-pMAPK
e
Col-0
fls2
bir3-2
Photon counts (x10⁵)
Time (min)
f
Mock
eBL
Hypocotyl length (rel. to ctrl.)
n=121
n=149
n=121
n=123
n=179
n=189
g
n=121
n=123
n=161
n=194
n=157
n=181
bak1-4
WT
bir3c
bak1-4/pBAK1::BAK1-mEOS3.2

376 **Extended Data Figure 9| Analyses of eBL and flg22 responsiveness in *BIR3* loss-of-function**
377 **mutants.**
378 **a**, **b**, and **c** Immunoprecipitation of FLS2 in Col-0 or *bir3-2* after treatment with 100 nM flg22 (a,
379 b, c) or corresponding mock solution (H_2O) for 5 min (**a, b, c**) or 20 nM flg22 and corresponding
380 mock solution (H_2O) for 2 min (**c**). Membranes were probed with anti-FLS2 or anti-BAK1. **c**d
381 Western blot analysis of MAPK phosphorylation in Arabidopsis seedlings treated for 5 min with
382 100 nM flg22. Membranes were probed with anti-FLS2 or anti-pERK42/44 (pMAPK) antibodies.
383 The same observations were made in 3 independent experiments. **e**, Time course analysis of ROS
384 production in 4-week-old Arabidopsis leaf discs treated with 100 nM flg22, values are mean ± se
385 of 4 independent experiments. **f** and **g**, Quantification of the hypocotyl length of 5-day-old
386 Arabidopsis seedlings grown on half MS medium containing 200 nM epi-Brassinolide (eBL) or
387 corresponding mock control solution (EtOH). Data points indicate measurements of the length of
388 individual hypocotyl relative to mock for each genotype, colors indicate independent experiments
389 Conditions sharing a letter are not significantly different in pairwise Wilcoxon test with Bonferroni
390 correction ($p<0.05$).
391

392 **Material and methods**

393 **Plant materials and growth**

394 *Arabidopsis thaliana* ecotype Columbia (Col-0) was used as WT control. Col-0/pFLS2::FLS2-
395 GFP[59], *bak1-4*[11], Col-0/pBRI1::BRI1-GFP[25], *fls2c*[60], *bir3-2*[14], Col-0/pBRI1::BRI1-GFP/BAK1-
396 mCherry[20], *bak1-4*/pBAK1::BAK1-GFP[26], Col-0/pBRI1::BRI1-mEOS3.2[61], were previously
397 described. Col-0/pFLS2::FLS2-GFP[59], was crossed with Col-0/pBAK1::BAK1-mCherry[62] to
398 obtain Col-0/pFLS2::FLS2-GFP/pBAK1::BAK1-mCherry. The following stable Arabopidopis
399 lines *fls2*/pUb::FLS2-mEOS3.2, *fls2*/pFLS2::FLS2-mEOS3.2, *bak1-4/*pBAK1::BAK1-
400 mEOS3.2, *bak1-4/*pUb::BAK1-mEOS3.2, *bak1-4/*pBAK1::BAK1^{D416N}-mEOS3.2, *bak1-*
401 *4/*pBAK1::BAK1$^{F60A/F144A}$-mEOS3.2, *bak1-4/*pUb::BAK1^{D122A}-mEOS3.2 and *bir3-2*/pUb::BIR3-
402 mEOS3.2 were generated by the transforming corresponding knock-out backgrounds via
403 floral dipping[63]. The transformants were selected on hygromycin (25 mg/L) to obtain
404 homozygous mono insertional lines and analyzed by western blotting using anti-BAK1 or
405 anti-FLS2 antibodies. Col-0/pFLS2::FLS2-GFP/pBAK1::BAK1-mCherry and Col-
406 0/pBRI1::BRI1-GFP/BAK1-mCherry were crossed with *fer-4*[64] to obtain *fer-4*/pFLS2::FLS2-
407 GFP/pBAK1::BAK1-mCherry and *fer-4*/pFLS2::FLS2-GFP/pBAK1::BAK1-mCherry. Col-
408 0/pFLS2::FLS2-GFP was crossed with *bak1-4*/pBAK1::BAK1-mEOS3.2 to obtain *bak1-*
409 *4*/pFLS2::FLS2-GFP/pBAK1::BAK1-mEOS3.2. *bir3-c/bak1-4*/pBAK1::BAK1-mEOS3.2 was
410 obtained by transforming *bak1-4/*pBAK1::BAK1-mEOS3.2 with CRISPR-Cas9 constructs
411 carrying a gRNA targeting *BIR3*. Transformants were selected based on seed coat
412 fluorescence, sequenced and T3 Cas9i-negative homozygous *BIR3* mutants were selected
413 for functional analyses. To analyse flg22-induced ROS production, plants were grown in
414 individual pots at 21 °C with a 10-h light photoperiod in environmentally controlled growth
415 rooms. For seedlings-based assays, seeds were surface-sterilized by incubating them in 0.1
416 % Tween20 in 70 % EtOH for 10 min, following 70 % EtOH for 10 min and 100% EtOH for 1
417 min. Seeds were stratified for 2 d in the dark at 4 °C and grown on half Murashige and Skoog
418 (MS) media supplemented with vitamins, 1 % sucrose and 0.8 % agar at 22 °C and a 16-h
419 light photoperiod.

420

421 **Molecular cloning, plant transformation and CRISPR-Cas9-mediated mutagenesis**

422 FLS2, BAK1 and BIR3 coding sequences and FLS2 and BAK1 promotors were obtained as
423 synthetic fragments (Genewiz) and cloned into the level 1 Golden Gate plasmid
424 pUC57_BB03 using BpiI[65,66]. The plasmid encoding for mEOS3.2 was previously described[32].
425 Nucleic acid fragments were assembled in the level 2 Golden Gate plasmid (BB24_LIIβ F 3-
426 4)[66]. *BIR3* gRNA for CRISPR Cas-mediated editing was designed using CHOPCHOP
427 (https://chopchop.cbu.uib.no/) and inserted into pAGM55261 using Golden Gate cloning[65].
428 All plasmids were verified by Sanger sequencing. The binary plasmids were transferred into

429 the *Agrobacterium tumefaciens* strain GV3101 for flower dip transformation of Arabidopsis
430 or transient transformation of *Nicotiana benthamiana* leaves.
431
432 **Brassinosteroid-sensitivity assay**
433 Brassinosteroid sensitivity assay was performed as previously described in[43]. Briefly, seeds
434 were surface-sterilized and individually placed in line on square Petri dishes containing half
435 MS 1 % sucrose, 0.8 % phytoagar, supplemented with 200 nM epi-brassinolide (Sigma,
436 Cat#E1641) or corresponding control solution (EtOH). The seeds were stratified at 4 °C for 2
437 d and then placed vertically in a growth chamber for 5 d. Hypocotyl length were measured
438 using Fiji[67].
439
440 **Co-immunoprecipitation**
441 Sample preparation and immunoprecipitation were performed as previously described[68].
442 Briefly, seedlings were grown on half MS media for 5 d and transferred to 6-well plates
443 containing liquid half MS to be cultivated for ten more days. Subsequently, seedlings from
444 10 wells were gathered and let rest for 1 h in liquid half MS. Seedlings were treated for 4 min
445 with either 20 nM or 100 nM flg22 or mock (distilled sterile water) and flash frozen in liquid
446 nitrogen. For protein extraction, tissues were grinded in liquid nitrogen and proteins were
447 isolated in 50 mM Tris-HCl pH 7.5, 150 mM NaCl, 10 % glycerol, 5 mM dithiothreitol, 1 %
448 protease inhibitor cocktail (Sigma-Aldrich), 2 mM Na2MoO4, 2.5 mM NaF, 1.5 mM activated
449 Na3VO4, 1 mM phenylmethanesulfonyl fluoride, and 0.5 % IGEPAL. For
450 immunoprecipitations, trueblot agarose beads (Rockland, 18-8816-33) were conjugated
451 with FLS2 antibodies (Agrisera, AS12 1857) and incubated with the crude protein extracts for
452 3 to 4 h at 4 °C. Subsequently, beads were washed three times with a washing buffer (50 mM
453 Tris-HCl pH 7.5, 150 mM NaCl, 1 mM phenylmethanesulfonyl fluoride, 0,1 % IGEPAL) before
454 adding 60 µL of a protein loading solution (6xSDS 10 % DTT) and incubating for 10 min at 90
455 °C. Analysis was carried out by SDS-PAGE and immunoblotting.
456
457 **Immunoblotting**
458 Protein samples were separated in 10 % bisacrylamide gels at 150 V for approximately 2
459 hours and transferred into activated PVDF membranes at 100 V for 90 min. Immunoblotting
460 was performed with antibodies diluted in blocking solution (5 % fat-free milk in TBS with 0.1
461 % [v/v] Tween-20). Antibodies used in this study were α-BAK1 (1:5000, Agrisera AS12 1858),
462 α-FLS2 (1:5000, Agrisera AS12 1857) or α-pMAPK (1:5000, pERK42/44 cell signal 9101S).
463 Blots were developed with Pierce ECL/ECL Femto Western Blotting Substrate (Thermo
464 Scientific). The following secondary antibody was used: anti-rabbit IgG (whole molecule)–
465 HRP (A0545, Sigma, dilution 1:10,000).
466

467 **Variable angle total internal reflection microscopy (VA-TIRFM)**
468 VA-TIRM imaging was performed as previously described in[32] Briefly, VA-TIRFM was operated
469 on a custom-build TIRFM set-up[61] equipped with an 100x objective NA 1.49 (Zeiss, 421190-
470 9800-000), four laser lines (405, 488, 561 and 642 nm), a polychromatic modulator (AOTF,
471 AA OPTO-ELECTRONIC) and a sCMOS camera (Hamamatsu Photonics, ORCA-Flash4.0 V2).
472 To ensure that the target laser power value always corresponds to the irradiance in the
473 sample plane, the power of each laser line was calibrated before each experiment using a
474 PM100D detector (Thorlabs). Five-day-old Arabidopsis seedlings or 3-week-old *N.*
475 *benthamiana* leave samples (28 to 34 h post Agrobacterium infiltration) were delicately
476 mounted between two coverslips (Epredia 24×50 mm #1) in liquid ½ MS medium and placed
477 on the specimen stage without additional weight. Images were acquired at 20 Hz frame rate
478 (50 ms), 6.66 Hz (150 ms) or 5 Hz (200 ms) for spt-PALM and photochromic reversion imaging
479 conditions.
480
481 **Single molecule imaging and analyses**
482 Photochromic reversion and spt-PALM imaging were performed as previously described[32].
483 Briefly, for photochromic reversion, mEOS3.2 was photoconverted, excited and kept in a
484 prolonged fluorescent state using 1000 µW 561nm laser power, 2-15 µW 405 nm laser power
485 and 1-30 µW 488 nm laser power. The emitted light was collected using 568 LP Edge Basic
486 Long-pass Filter, 584/40 ET Band-pass filters (AHF analysentechnik AG) and recorded from
487 a 51.2 x 51.2 µm region of interest, 100 nm pixel size. Track reconstruction and analysis was
488 carried out as previously described[32]. To ensure bona-fide single-molecule tracking we
489 analyzed frames with relatively low molecule density (ca. 0.1 – 1 molecule per μm^2). We used
490 the plugin TrackMate[69] in Fiji[67] to reconstruct single molecule trajectories. Single particles
491 were segmented frame-by-frame by applying a Laplacian of Gaussian (LoG) filter and
492 estimated particle size of 0.3 µm with a Quality threshold of 30. Individual single particles
493 were localized with sub-pixel resolution using a built-in quadratic fitting scheme. Single-
494 particle trajectories were reconstructed using a simple linear assignment problem[70] with a
495 maximal linking distance of 0.4 µm and a 2 frames-gap-closing maximum. The coordinates
496 of the single particle trajectories were then further analyzed using a custom-made python
497 script to calculate the mean square displacement (MSD) and diffusion coefficient (D) in
498 batch mode. Only tracks with a minimum of five localizations were kept for analysis. The
499 MSD and diffusion coefficient was calculated based on the first four time points of each
500 trajectory as previously described[71]. Single molecule trajectories clustering was performed
501 using nastic[35] with the following threshold, time = 20 s, radius factor = 1.2, minimum
502 trajectories = 3, size screen = 0.15 µm. Spatial arrests were analyzed using CASTA, with the
503 default minimum track length of 25 timepoints[32] (https://pypi.org/project/casta/).
504

505 **Enhanced super-resolution radial fluctuations (eSRRF)**
506 Stable transgenic lines expressing BRI1-GFP, BAK1-GFP or FLS2-GFP were imaged by VA-
507 TIRFM as described above at 5 Hz (200 ms) frame rate. Super resolved images were
508 reconstructed using eSRRF[29] in Fiji[67]. Stream VA-TIRFM acquisitions were processed using
509 the following parameters that were defined by iterative parameter sweep[29]: magnification =
510 6, radius = 3, sensitivity = 3 and frames = 100. The average (AVG) reconstructions of BRI1-
511 GFP, BAK1-GFP and FLS2-GFP plasma membrane organization were segmented and
512 analysed using Nanonet, a custom-made automated analysis pipeline
513 (https://github.com/NanoSignalingLab/NanoNet), providing nanodomain density and image
514 wide spatial clustering index (iSCI) based on predicted localization density.
515
516 **Measurement of reactive oxygen species production**
517 Arabidopsis plants were grown in individual pots at 21 °C with a 10-h light photoperiod in
518 environmentally controlled growth rooms. Leaf discs (4 mm in diameter) were excised from
519 3- to 4-week-old plants and incubated in 96-well plates containing sterile distilled water
520 overnight. The following day, water was replaced with a solution containing 0.5 µM L-012 and
521 20 µg/mL horseradish peroxidase (HRP, Sigma Aldrich) and 100 nM flg22 or control (water).
522 Luminescence was measured using a microplate reader (Promega Glomax navigator) over a
523 period of 60 min.
524
525 **Particle based simulations**
526 Computational simulations of single particles were performed using the Smoldyn software
527 (version 2.75)[53], and a custom-made python script. We simulated a 2D space of 10 μm^2 with
528 periodic boundaries conditions to avoid edge effects. We imposed a triangular mesh with an
529 average compartment size corresponding to the size FLS2 nanoclusters obtained by NASTIC.
530 To simulate FLS2, BAK1 and BIR3 molecular diffusion we provided as input data the
531 instantaneous diffusion coefficient (D) measured by photochromic reversion. For each step
532 and each molecule, a new displacement is randomly chosen from normally distributed
533 possible displacements. The probability of molecule diffusion across compartment
534 boundaries was defined as 0.00001 for FLS2, 0.00001 for BIR3 and 1 for BAK1. To simulate
535 molecule binding kinetics, we used the Kon and Koff of flg22-bound FLS2 to BAK1[54] and the
536 Kd of BAK1 to BIR3[13] converted into binding and unbinding radii. Simulations were run using
537 a delta t of 0.0001s to ensure that the spatial resolution was smaller than the geometric
538 features and the characteristic time scale of the system for each possible reaction. The
539 initial location of each molecule was randomized for each simulation. To analyse the effect
540 of BIR3 on BAK1 localization we monitored the number of BAK1 molecules within FLS2
541 nanodomains every 5 ms for 300 s. To simulate flg22 perception, FLS2 molecules were

converted to flg22-bound FLS2 molecules after 120 s and FLS2-flg22/BAK1 complexes were measured every 50 ms for 300 s.

References

1 DeFalco, T. A. & Zipfel, C. Molecular mechanisms of early plant pattern-triggered immune signaling. *Mol Cell* **81**, 3449–3467 (2021). https://doi.org/10.1016/j.molcel.2021.07.029

2 Smakowska-Luzan, E. *et al.* An extracellular network of Arabidopsis leucine-rich repeat receptor kinases. *Nature* **553**, 342–346 (2018). https://doi.org/10.1038/nature25184

3 Özkan, E. *et al.* An extracellular interactome of immunoglobulin and LRR proteins reveals receptor-ligand networks. *Cell* **154**, 228–239 (2013). https://doi.org/10.1016/j.cell.2013.06.006

4 Monaghan, J. & Zipfel, C. Plant pattern recognition receptor complexes at the plasma membrane. *Curr Opin Plant Biol* **15**, 349–357 (2012). https://doi.org/10.1016/j.pbi.2012.05.006

5 Lemmon, M. A. & Schlessinger, J. Cell signaling by receptor tyrosine kinases. *Cell* **141**, 1117–1134 (2010). https://doi.org/10.1016/j.cell.2010.06.011

6 Shiu, S. H. & Bleecker, A. B. Receptor-like kinases from Arabidopsis form a monophyletic gene family related to animal receptor kinases. *Proc Natl Acad Sci U S A* **98**, 10763–10768 (2001). https://doi.org/10.1073/pnas.181141598

7 Li, J. & Chory, J. A Putative Leucine-Rich Repeat Receptor Kinase Involved in Brassinosteroid Signal Transduction. *Cell* **90**, 929–938 (1997). https://doi.org/https://doi.org/10.1016/S0092-8674(00)80357-8

8 Jinn, T. L., Stone, J. M. & Walker, J. C. HAESA, an Arabidopsis leucine-rich repeat receptor kinase, controls floral organ abscission. *Genes Dev* **14**, 108–117 (2000).

9 Gómez-Gómez, L., Bauer, Z. & Boller, T. Both the extracellular leucine-rich repeat domain and the kinase activity of FSL2 are required for flagellin binding and signaling in Arabidopsis. *Plant Cell* **13**, 1155–1163 (2001).

10 Nam, K. H. & Li, J. BRI1/BAK1, a receptor kinase pair mediating brassinosteroid signaling. *Cell* **110**, 203–212 (2002). https://doi.org/10.1016/s0092-8674(02)00814-0

11 Chinchilla, D. *et al.* A flagellin-induced complex of the receptor FLS2 and BAK1 initiates plant defence. *Nature* **448**, 497–500 (2007). https://doi.org/10.1038/nature05999

12 Ma, C. *et al.* Structural basis for BIR1-mediated negative regulation of plant immunity. *Cell Research* **27**, 1521–1524 (2017). https://doi.org/10.1038/cr.2017.123

13 Hohmann, U., Nicolet, J., Moretti, A., Hothorn, L. A. & Hothorn, M. The SERK3 elongated allele defines a role for BIR ectodomains in brassinosteroid signalling. *Nat Plants* **4**, 345–351 (2018). https://doi.org/10.1038/s41477-018-0150-9

14 Imkampe, J. *et al.* The Arabidopsis Leucine-Rich Repeat Receptor Kinase BIR3 Negatively Regulates BAK1 Receptor Complex Formation and Stabilizes BAK1. *Plant Cell* **29**, 2285–2303 (2017). https://doi.org/10.1105/tpc.17.00376

15 Großeholz, R. *et al.* Specifying the role of BAK1-interacting receptor-like kinase 3 in brassinosteroid signaling. *J Integr Plant Biol* **62**, 456–469 (2020). https://doi.org/10.1111/jipb.12803

16 Bücherl, C. A. *et al.* Plant immune and growth receptors share common signalling components but localise to distinct plasma membrane nanodomains. *Elife* **6** (2017). https://doi.org/10.7554/eLife.25114

17 Gronnier, J. *et al.* Regulation of immune receptor kinase plasma membrane nanoscale organization by a plant peptide hormone and its receptors. *eLife* **11**, e74162 (2022). https://doi.org/10.7554/eLife.74162

18 McKenna, J. F. *et al.* The cell wall regulates dynamics and size of plasma-membrane nanodomains in Arabidopsis. *Proceedings of the National Academy of Sciences* **116**, 12857–12862 (2019). https://doi.org/doi:10.1073/pnas.1819077116

19 Cui, Y. *et al.* Sterols regulate endocytic pathways during flg22-induced defense responses in Arabidopsis. *Development* **145** (2018). https://doi.org/10.1242/dev.165688

20 Hutten, S. J. *et al.* Visualization of BRI1 and SERK3/BAK1 Nanoclusters in Arabidopsis Roots. *PLOS ONE* **12**, e0169905 (2017). https://doi.org/10.1371/journal.pone.0169905

21 Ma, Z., Xie, Y., Chng, C.-P., Huang, C. & Miao, Y. Synthetic FLS2 receptor oligomer boosts plant innate immunity. *bioRxiv*, 2025.2001.2027.634983 (2025). https://doi.org/10.1101/2025.01.27.634983

22 Jaillais, Y. *et al.* Guidelines for naming and studying plasma membrane domains in plants. *Nat Plants* **10**, 1172–1183 (2024). https://doi.org/10.1038/s41477-024-01742-8

23 Liu, M. J. *et al.* Extracellular pectin-RALF phase separation mediates FERONIA global signaling function. *Cell* **187**, 312–330.e322 (2024). https://doi.org/10.1016/j.cell.2023.11.038

24 Robatzek, S., Chinchilla, D. & Boller, T. Ligand-induced endocytosis of the pattern recognition receptor FLS2 in Arabidopsis. *Genes Dev* **20**, 537–542 (2006). https://doi.org/10.1101/gad.366506

25 Geldner, N., Hyman, D. L., Wang, X., Schumacher, K. & Chory, J. Endosomal signaling of plant steroid receptor kinase BRI1. *Genes Dev* **21**, 1598–1602 (2007). https://doi.org/10.1101/gad.1561307

26 Ntoukakis, V., Schwessinger, B., Segonzac, C. & Zipfel, C. Cautionary Notes on the Use of C-Terminal BAK1 Fusion Proteins for Functional Studies. *The Plant Cell* **23**, 3871–3878 (2011). https://doi.org/10.1105/tpc.111.090779

27 Tokunaga, M., Imamoto, N. & Sakata-Sogawa, K. Highly inclined thin illumination enables clear single-molecule imaging in cells. *Nat Methods* **5**, 159–161 (2008). https://doi.org/10.1038/nmeth1171

28 Konopka, C. A. & Bednarek, S. Y. Variable-angle epifluorescence microscopy: a new way to look at protein dynamics in the plant cell cortex. *The Plant Journal* **53**, 186–196 (2008). https://doi.org/https://doi.org/10.1111/j.1365-313X.2007.03306.x

29 Laine, R. F. *et al.* High-fidelity 3D live-cell nanoscopy through data-driven enhanced super-resolution radial fluctuation. *Nature Methods* **20**, 1949–1956 (2023). https://doi.org/10.1038/s41592-023-02057-w

30 Wang, L. *et al.* Spatiotemporal Dynamics of the BRI1 Receptor and its Regulation by Membrane Microdomains in Living Arabidopsis Cells. *Molecular Plant* **8**, 1334–1349 (2015). https://doi.org/https://doi.org/10.1016/j.molp.2015.04.005

31 Tran, T. M. *et al.* The bacterial quorum sensing signal DSF hijacks Arabidopsis thaliana sterol biosynthesis to suppress plant innate immunity. *Life Sci Alliance* **3** (2020). https://doi.org/10.26508/lsa.202000720

32 von Arx, M., Xhelilaj, K., Schulz, P., zur Oven-Krockhaus, S. & Gronnier, J. Photochromic reversion enables long-term tracking of single molecules in living plants. *bioRxiv*, 2024.2004.2010.585335 (2024). https://doi.org/10.1101/2024.04.10.585335

33 Zhang, M. *et al.* Rational design of true monomeric and bright photoactivatable fluorescent proteins. *Nature Methods* **9**, 727–729 (2012). https://doi.org/10.1038/nmeth.2021

34 Grefen, C. *et al.* A ubiquitin-10 promoter-based vector set for fluorescent protein tagging facilitates temporal stability and native protein distribution in transient and stable expression studies. *Plant J* **64**, 355–365 (2010). https://doi.org/10.1111/j.1365-313X.2010.04322.x

35 Wallis, T. P. *et al.* Super-resolved trajectory-derived nanoclustering analysis using spatiotemporal indexing. *Nature Communications* **14**, 3353 (2023). https://doi.org/10.1038/s41467-023-38866-y

36 Low-Nam, S. T. *et al.* ErbB1 dimerization is promoted by domain co-confinement and stabilized by ligand binding. *Nat Struct Mol Biol* **18**, 1244–1249 (2011). https://doi.org/10.1038/nsmb.2135

37 Niwa, F. *et al.* Gephyrin-Independent GABAAR Mobility and Clustering during Plasticity. *PLOS ONE* **7**, e36148 (2012). https://doi.org/10.1371/journal.pone.0036148

38 Sako, Y., Minoghchi, S. & Yanagida, T. Single-molecule imaging of EGFR signalling on the surface of living cells. *Nature Cell Biology* **2**, 168–172 (2000). https://doi.org/10.1038/35004044

39 Wang, Y. *et al.* Regulation of EGFR nanocluster formation by ionic protein-lipid interaction. *Cell Research* **24**, 959–976 (2014). https://doi.org/10.1038/cr.2014.89

40 Schulze, B. *et al.* Rapid heteromerization and phosphorylation of ligand-activated plant transmembrane receptors and their associated kinase BAK1. *J Biol Chem* **285**, 9444–9451 (2010). https://doi.org/10.1074/jbc.M109.096842

41 Delesalle, C., Vert, G. & Fujita, S. The cell surface is the place to be for brassinosteroid perception and responses. *Nature Plants* **10**, 206–218 (2024). https://doi.org/10.1038/s41477-024-01621-2

42 Hurst, C. H. *et al.* S-acylation stabilizes ligand-induced receptor kinase complex formation during plant pattern-triggered immune signaling. *Current Biology* **33**, 1588–1596.e1586 (2023). https://doi.org/10.1016/j.cub.2023.02.065

43 Biermann, D. *et al.* A RALF-brassinosteroid signaling circuit regulates Arabidopsis hypocotyl cell shape. *Current Biology* **35**, 5002–5017.e5005 (2025). https://doi.org/10.1016/j.cub.2025.09.016

44 Stegmann, M. *et al.* The receptor kinase FER is a RALF-regulated scaffold controlling plant immune signaling. *Science* **355**, 287–289 (2017). https://doi.org/doi:10.1126/science.aal2541

45 Sun, Y. *et al.* Structural basis for flg22-induced activation of the Arabidopsis FLS2-BAK1 immune complex. *Science* **342**, 624–628 (2013). https://doi.org/10.1126/science.1243825

46 Santiago, J. *et al.* Mechanistic insight into a peptide hormone signaling complex mediating floral organ abscission. *eLife* **5**, e15075 (2016). https://doi.org/10.7554/eLife.15075

47 Santiago, J., Henzler, C. & Hothorn, M. Molecular Mechanism for Plant Steroid Receptor Activation by Somatic Embryogenesis Co-Receptor Kinases. *Science* **341**, 889–892 (2013). https://doi.org/doi:10.1126/science.1242468

48 Sun, Y. *et al.* Structure reveals that BAK1 as a co-receptor recognizes the BRI1-bound brassinolide. *Cell Research* **23**, 1326–1329 (2013). https://doi.org/10.1038/cr.2013.131

49 Schwessinger, B. *et al.* Phosphorylation-Dependent Differential Regulation of Plant Growth, Cell Death, and Innate Immunity by the Regulatory Receptor-Like Kinase BAK1. *PLOS Genetics* **7**, e1002046 (2011). https://doi.org/10.1371/journal.pgen.1002046

50 Wang, X. *et al.* Sequential Transphosphorylation of the BRI1/BAK1 Receptor Kinase Complex Impacts Early Events in Brassinosteroid Signaling. *Developmental Cell* **15**, 220–235 (2008). https://doi.org/10.1016/j.devcel.2008.06.011

51 Halter, T. *et al.* The leucine-rich repeat receptor kinase BIR2 is a negative regulator of BAK1 in plant immunity. *Curr Biol* **24**, 134–143 (2014). https://doi.org/10.1016/j.cub.2013.11.047

52 Guzmán-Benito, I. *et al.* The immune repressor BIR1 contributes to antiviral defense and undergoes transcriptional and post-transcriptional regulation during viral infections. *New Phytol* **224**, 421–438 (2019). https://doi.org/10.1111/nph.15931

53 Andrews, S. S. Smoldyn: particle-based simulation with rule-based modeling, improved molecular interaction and a library interface. *Bioinformatics* **33**, 710–717 (2016). https://doi.org/10.1093/bioinformatics/btw700

54 Okuda, S. *et al.* Molecular mechanism for the recognition of sequence-divergent CIF peptides by the plant receptor kinases GSO1/SGN3 and GSO2. *Proceedings of the National Academy of Sciences* **117**, 2693–2703 (2020). https://doi.org/doi:10.1073/pnas.1911553117

55 Sun, Y. *et al.* A Leucine-Rich Repeat Receptor-like Kinase TaBIR1 Contributes to Wheat Resistance against Puccinia striiformis f. sp. tritici. *International Journal of Molecular Sciences* **24**, 6438 (2023).

56 Liu, F. *et al.* BAK1 protects the receptor-like kinase BIR2 from SNIPER2a/b-mediated degradation to promote pattern-triggered immunity in Nicotiana benthamiana. *The Plant Cell* **35**, 3566–3584 (2023).

57 Guo, J. *et al.* OsBIR3 maintains the homeostasis of OsBRI1, OsREM4.1, and Brd2 protein levels in brassinosteroid pathways in rice. *Plant Biotechnology Journal* **23**, 3024–3040 (2025). https://doi.org/https://doi.org/10.1111/pbi.70128

58 You, C. *et al.* Receptor dimer stabilization by hierarchical plasma membrane microcompartments regulates cytokine signaling. *Science Advances* **2**, e1600452 (2016). https://doi.org/doi:10.1126/sciadv.1600452

59 Göhre, V. *et al.* Plant Pattern-Recognition Receptor FLS2 Is Directed for Degradation by the Bacterial Ubiquitin Ligase AvrPtoB. *Current Biology* **18**, 1824–1832 (2008). https://doi.org/10.1016/j.cub.2008.10.063

60 Zipfel, C. *et al.* Bacterial disease resistance in Arabidopsis through flagellin perception. *Nature* **428**, 764–767 (2004). https://doi.org/10.1038/nature02485

61 Rohr, L. *et al.* OneFlowTraX: a user-friendly software for super-resolution analysis of single-molecule dynamics and nanoscale organization. *Frontiers in Plant Science* **Volume 15 - 2024** (2024). https://doi.org/10.3389/fpls.2024.1358935

62 Bücherl, C. A. *et al.* Visualization of BRI1 and BAK1(SERK3) Membrane Receptor Heterooligomers during Brassinosteroid Signaling *Plant Physiology* **162**, 1911–1925 (2013). https://doi.org/10.1104/pp.113.220152

63 Clough, S. J. & Bent, A. F. Floral dip: a simplified method for Agrobacterium-mediated transformation of Arabidopsis thaliana. *Plant J* **16**, 735–743 (1998). https://doi.org/10.1046/j.1365-313x.1998.00343.x

64 Duan, Q., Kita, D., Li, C., Cheung, A. Y. & Wu, H. M. FERONIA receptor-like kinase regulates RHO GTPase signaling of root hair development. *Proc Natl Acad Sci U S A* **107**, 17821–17826 (2010). https://doi.org/10.1073/pnas.1005366107

65 Engler, C. *et al.* A Golden Gate Modular Cloning Toolbox for Plants. *ACS Synthetic Biology* **3**, 839–843 (2014). https://doi.org/10.1021/sb4001504

66 Binder, A. *et al.* A modular plasmid assembly kit for multigene expression, gene silencing and silencing rescue in plants. *PLoS One* **9**, e88218 (2014). https://doi.org/10.1371/journal.pone.0088218

67 Schindelin, J. *et al.* Fiji: an open-source platform for biological-image analysis. *Nature Methods* **9**, 676–682 (2012). https://doi.org/10.1038/nmeth.2019

68 Kadota, Y. *et al.* Direct regulation of the NADPH oxidase RBOHD by the PRR-associated kinase BIK1 during plant immunity. *Mol Cell* **54**, 43–55 (2014). https://doi.org/10.1016/j.molcel.2014.02.021

69 Ershov, D. *et al.* TrackMate 7: integrating state-of-the-art segmentation algorithms into tracking pipelines. *Nature Methods* **19**, 829–832 (2022). https://doi.org/10.1038/s41592-022-01507-1

70 Jaqaman, K. *et al.* Robust single-particle tracking in live-cell time-lapse sequences. *Nature Methods* **5**, 695–702 (2008). https://doi.org/10.1038/nmeth.1237

71 Saxton, M. J. & Jacobson, K. Single-particle tracking: applications to membrane dynamics. *Annu Rev Biophys Biomol Struct* **26**, 373–399 (1997). https://doi.org/10.1146/annurev.biophys.26.1.373